Convective Dissolution of Carbon Dioxide in Deep Saline Aquifers: Insights from Engineering a High-Pressure Porous Visual Cell

Saeed Mahmoodpour,[1] Behzad Rostami[1,*] Mohamad Reza Soltanian,[2,3] and Mohammad Amin Amooie[4,†]

[1] *Institute of Petroleum Engineering, College of Engineering, University of Tehran, Iran*

[2] *Department of Geology, University of Cincinnati, Cincinnati, Ohio 45221, USA*

[3] *Department of Chemical and Environmental Engineering, University of Cincinnati, Cincinnati, Ohio 45221, USA*

[4] *Department of Chemical Engineering, Massachusetts Institute of Technology, Cambridge, Massachusetts 02139, USA*

We present the first experiments of dissolution-driven convection of carbon dioxide (CO_2) in a confined brine-saturated porous medium at high pressures. We designed an alternative cell that allows for both visual and quantitative analyses, and address the effects of free-phase CO_2 and brine composition on convective dissolution. The visual examination of the gas volume combined with the measurement of pressure, which both evolve with dissolution, enables us to yield insights into the dynamics of convection in conditions that more closely reflect the geologic conditions. We find and analyze different dissolution events, including diffusive, early, and late convection and shutdown regimes. Our experiments reveal that in intermediate regimes, a so-called "quasisteady" state actually never happens. Dissolution flux continuously decreases in this regime, which is due to a negative feedback loop: the rapid reduction of pressure following convective dissolution (allowed by gas expansion), in turn, decreases the solubility of CO_2 at the gas-brine interface and thus the instability strength. We introduce an alternative scaling factor that not only compensates the flux reduction but also the nonlinearities that arise from different salt types. We present robust scaling relations for the compensated flux and for the transition times between consecutive regimes in systems with NaCl (Ra $\sim$ 3271–4841) and NaCl + $CaCl_2$ mixtures (Ra $\sim$ 2919–4283). We also find that NaCl + $CaCl_2$ mixtures enjoy a longer intermediate period before the shutdown of dissolution, but with a lower dissolution flux, as compared to NaCl brines. The results provide an alternative perspective into how the presence of two separate phases in a closed system as well as different salt types may affect the predictive powers of our experiments and models for both the short- and long-term dynamics of convective dissolution in porous media.

I. INTRODUCTION

Natural convection emerges when a fluid with higher density overlays a lower density fluid. Convection can significantly enhance the transport of mass, heat, and energy, and it is ubiquitous in many natural and industrial areas, including weather systems [1,2], plate tectonics [3,4], oceanic currents [5], sea water and groundwater aquifers [6], free air cooling [7], electronic devices [8–10], solar ponds [11], and microfluidic systems [12]. In the context of porous media, natural convection has applications in geothermal energy production [13], heat exchangers [14], sand separation from oil [15], and many others.

The convection in porous media has recently received renewed attention because of its importance in carbon dioxide (CO_2) sequestration in underground formations as one of the most promising options to stabilize atmospheric CO_2 concentrations and hence mitigate the global climate change [16]. Deep saline aquifers have been recognized as the primary target among storage repositories beneath the Earth's surface, mainly owing to their favorable chemistry, porosity, temperature, pressure, huge capacity, and wide distribution all over the world [17]. Natural convection controls the dissolution of injected CO_2 into underlying brine, which is a key mechanism for the permanent and efficient trapping of CO_2. Our goal here is to study the dynamics of convective CO_2 dissolution in brine, which not only gives insights into the short- and long-term fate of CO_2 injected into the subsurface but may also contribute to

*brostami@ut.ac.ir
†amooie@mit.edu

the further understanding of convection dynamics in other fields.

During the geological sequestration of CO_2 in deep brine-bearing formations (i.e., saline aquifers), buoyant CO_2 rises upward until it is confined by an impermeable caprock while spreading laterally beneath. This structurally trapped CO_2 is, however, susceptible to leak back to the surface due to the existence of small fractures or faults in the seal. Moreover, in the injection stage, the caprock integrity may be compromised by the reservoir overpressurization, which would induce new fractures or cause slip along preexisting faults in the seal [18,19].

CO_2 dissolution in brine (or groundwater) is an important trapping mechanism toward permanent storage of CO_2, which would reduce the risk of leakage from imperfect or compromised caprocks [18,20–25]. The diffusion of CO_2 molecules into brine initiates the dissolution process [26,27], which results in a diffusive boundary layer that is more dense than the underlying formation brine and hence prone to density-driven instabilities [27]. Beyond a critical thickness of this boundary layer, fingering instabilities form. As these instabilities grow, they migrate toward the formation bottom through convection while carrying further dissolved CO_2 away from the seal. The underlying lighter fluid at lower CO_2 concentrations rises upward at the same time, thereby sharpening the CO_2 concentration gradient at the gas-brine interface that accelerates the dissolution rate [28–31]. An estimation of the dissolution flux helps to constrain the amount of CO_2 that will remain in solution in the subsurface and the amount that is prone to escape.

The dissolution and mixing of CO_2 has been well studied in idealized systems of porous convection. The two-phase fluid system that forms following the injection of CO_2, where free-phase (gaseous) CO_2 overlays the brine-saturated layer with a dynamic and temporally evolving interface in between, is typically simplified into a one-phase system through one of the following approaches. Analog fluid systems are used as an alternative, where the two-phase CO_2-brine system is replaced with a single-phase two-layer system composed of water and suitable fluid [e.g., methanol and ethylene-glycol (MEG) or propylene glycol (PPG)] that is miscible with water. As such, the analog fluid systems result in a nonmonotonic density profile for the mixture and cannot represent the partial miscibility [32,33], density and viscosity profiles, or instability strength, and thus the underlying dynamics of actual CO_2-brine systems [34–36]. The two-phase system models can also be simplified by including only the porous layer below the gas-brine interface and representing this interface by (i) a top boundary fixed at CO_2 saturation (e.g., Refs. [37–40]) or (ii) a top boundary of constant flux of CO_2 at a low rate such that CO_2 goes into the solution immediately [26,27,41].

In the simplified, one-phase systems mentioned above, the dissolution process after the onset of convection can be summarized as follows. First, the fingers grow independently and descend to the bottom of the aquifer with small lateral interactions [39]. However, as time goes on, the fingers start to merge with their neighboring fingers and create stronger fingers. At this time, the dissolution flux (or mixing rate) increases with time in a flux-growth (FG) (or dissipation-growth) regime [42,43]. After the convective regime has developed, the quasisteady state regime starts [43], during which the convective flow brings the fresh brine to the gas-brine interface and the process continues in a quasisteady regime until the brine brought to the gas-brine interface begins to contain dissolved CO_2. The latter can happen some time after the descending fingers reach the bottom. The dissolution process then shifts to the shutdown regime and continues to reach the maximum dissolution capacity of the system at the given pressure, temperature, and salinity [44]. For completeness, we gather and summarize the scaling results from previous numerical and experimental studies for these regimes in Table I. These results are usually based on the Sherwood number (Sh) and the Rayleigh number (Ra) as

$$\text{Ra} = \frac{\Delta\rho k g H}{\mu D \varphi}, \tag{1}$$

$$\text{Sh} = \frac{H}{D\varphi\Delta c}F, \tag{2}$$

where $\Delta\rho$ (kg/m^3), k (m^2), g (m/s^2), H (m), μ (kg/m s^{-1}), D (m^2/s), φ, Δc (mol/m^3), and F (mol/m^2 s) are respectively the density difference, permeability, gravitational acceleration, depth, viscosity, diffusion coefficient, porosity, concentration gradient, and dissolution flux. Here, Ra is always obtained based on initial conditions where the above parameters are constants.

What all these idealized systems have in common is that they consider only a single-phase system where free-phase CO_2 as well as multiphase processes that could affect the interface dynamics, partial pressure evolution for each phase, CO_2 solubility, and the associated density increases are absent [13,15,16,23,24]. In addition, scarce CO_2-brine or CO_2-water experiments have been conducted recently either in blind cells [23,24,52,55] or low-pressure Hele-Shaw cells [54,56]. There is not a combination of visual and quantitative data in the literature on the convection dynamics of truly two-phase CO_2-brine systems in porous media that could represent the geological carbon sequestration in deep, high-pressure saline aquifers. Here, we present the convective dissolution behavior of CO_2 in brine via engineering a high-pressure porous visual cell that allows for both qualitative and quantitative insights into the different flow regimes and the underlying two-phase fluid dynamics. Our visual inspection and scaling analysis of density-driven flow following the dissolution

TABLE I. A summary of scaling relations for estimating dissolution flux.

Reference	System	Regime	Analysis method	Ra range	Equation
[45]	...	Quasisteady	Numerical	...	$\mathrm{Sh} = 0.017\mathrm{Ra}$
[46]	MEG[a]-water	Quasisteady	Experimental numerical	2×10^3–6×10^5	$\mathrm{Sh} = 0.12\mathrm{Ra}^{0.84}$
[38]	...	Quasisteady	Numerical	...	$F = 0.017(c_0 k \Delta \rho g / \mu)$
[34]	PPG[b]-water	Quasisteady	Experimental	6×10^3–9×10^4	$\mathrm{Sh} = 0.045\mathrm{Ra}^{0.76}$
[47]	...	Quasisteady	Numerical	...	$F = 0.02(c_0 k \Delta \rho g / \mu)$
[35]	...	Quasisteady	Numerical	5×10^3–3×10^4	$F = a(c_0 k \Delta \rho g / \mu)$
[48]	...	Quasisteady	Numerical	1×10^3–8×10^3	$\mathrm{Sh} = 0.0794\mathrm{Ra}^{0.832}$
[49]	PPG[b]-water	Quasisteady	Experimental	5×10^3–1×10^5	$\mathrm{Sh} = 0.037\mathrm{Ra}^{0.84}$
[50]	...	Quasisteady	Numerical	...	$F = 0.021(c_0 k \Delta \rho g / \mu)$
[51]	...	Quasisteady	Numerical	...	$F = 0.017\sqrt{k_v k_h}(c_0 \Delta \rho g / \mu)$
[52]	CO_2-brine (NaCl)	Quasisteady	Experimental	182–20860	$\mathrm{Sh} = 0.0228\mathrm{Ra}^{0.7897}$
[42]	...	Quasisteady	Numerical	2×10^3–5×10^5	$F = 0.017(c_0 k \Delta \rho g / \mu)$
		Shutdown			$\mathrm{Sh} = 16.8/[0.73\,(t/\mathrm{Ra} - 16) + 31.5]^2$
[21]	...	Quasisteady	Numerical	...	$F = (0.018, 0.019)\,(c_0 k \Delta \rho g / \mu)$
[53]	NaCl solution-MEG	Quasisteady	Experimental	2600–16036	$\mathrm{Sh} = 0.13\mathrm{Ra}^{0.93}$
[40]	...	Quasisteady	Numerical	1×10^3–2×10^4	$F = 0.017\sqrt{k_v k_h}(c_0 \Delta \rho g / \mu)$
		Shutdown			$\mathrm{Sh} = 4a\,(k_v/k_h)^{a'}/\left[1 + 4a\,(k_v/k_h)^{a'}\,t/\mathrm{Ra}\right]^2$
[54]	CO_2-water	Quasisteady	Experimental	709–9627	$F = 0.021\Delta \rho g \cos(\theta)\,kc_0/\mu$
[23]	CO_2-water	FG	Experimental numerical	2093–16256	$F = a' t^{0.5}$
		Quasisteady			$F = a(c_0 k \Delta \rho g / \mu \varphi)$
		Shutdown			$F = a' t^{-1.75}$
[43]	...	Quasisteady	Numerical	1×10^4–5×10^4	$\mathrm{Sh} = 0.0168\mathrm{Ra}_0/(0.0168 a t_a + 1)^2$
		Shutdown			$\mathrm{Sh} = 0.0317\mathrm{Ra}_0/[0.0317\,(1 + a)\,t_a + 0.861]^2$

[a]Methanol and ethylene-glycol.
[b]Propylene glycol.
[c]a, a' are constant values.

of free-phase CO_2 in an underlying porous layer more closely reflects the fate of injected CO_2 under a geologic trap and will advance our fundamental understanding and predictive capabilities of CO_2 sequestration.

Saline aquifers can either be open, allowing for the compensation of pressure changes by brine migration, or closed (fault bounded), naturally not allowing for pressure change compensation [57]. In closed aquifers, brine saturation with CO_2 [39,58] and likely pressure drop in the CO_2 free phase [43] would limit the CO_2 dissolution in brine. Wen *et al.* [43] showed numerically that in closed aquifers the dissolution flux in the intermediate, supposedly quasisteady regime is actually not constant, and they suggested the following relation between the dimensionless dissolution flux in closed and open aquifers [43]:

$$F_{\mathrm{closed}} \approx F_{\mathrm{open}} C_s^2, \qquad (3)$$

where C_s represents the dimensionless (with respect to initial conditions) equilibrium concentration of CO_2 at the interface with brine. In this study, a confined high-pressure cell is designed and implemented in an experimental setup to investigate the complex behavior of CO_2 dissolution in closed aquifers. We show that our experimental findings attest to the general validity of the numerical results of

Wen *et al.* [43], particularly in terms of the dynamics of the aforesaid intermediate regime. For consistency, we still refer to this regime simply as the "quasisteady regime" despite the nonconstant behavior of dissolution flux during this period. Most previous studies, moreover, have considered only pure water (i.e., with no salinity) rather than brine. The latter is typically composed of different salts [59]. Data on brine composition show the dominance of chloride (Cl^-) and sodium (Na^+) ions. Among other cations, calcium (Ca^{2+}) is the most frequent one [24, 53,60–66]. The transition time between the dissolution regimes controls the total amount of dissolved CO_2 with time. One of our goals here is to provide scaling relations for transition times between dissolution regimes and for dissolution fluxes in CO_2 brine systems that contain NaCl and NaCl + $CaCl_2$ mixtures. These relations are helpful for examining system behavior in more realistic conditions where a mixture of salts constitutes the formation brine.

The present study is organized as follows. Section II presents the methodology and the description of the experimental setup and details of the implemented tests. Results are provided and analyzed in Sec. III. In the first part of this section, the dynamic of the dissolution process is examined through the visual data. In the second part, quantitative data (pressure data as well as dissolution

TABLE II.   The details of experimental tests with their order number, brine composition, permeability, Rayleigh value, initial pressure, and diffusion coefficient. The details of the correlations that are used to calculate Ra are provided in Appendixes A–E.

Test number	Brine composition, molal based (m)	Permeability (darcy)	Initial Ra	Initial pressure (psi)	Diffusion ($10^9 \, m^2/s$)
1	2 NaCl	550	4444	523.1 (3.61 MPa)	3.8
2	2 NaCl	400	3272	511.2 (3.52 MPa)	3.7
3	1 NaCl	550	4841	535.3 (3.69 MPa)	5
4	1 NaCl	400	3514	510.6 (3.52 MPa)	4.9
5	1.6 NaCl + 0.2 $CaCl_2$	550	3893	512.7 (3.53 MPa)	4.2
6	1.6 NaCl + 0.2 $CaCl_2$	400	2919	514.7 (3.55 MPa)	4.1
7	0.8 NaCl + 0.1 $CaCl_2$	550	4283	502.6 (3.47 MPa)	5.3
8	0.8 NaCl + 0.1 $CaCl_2$	400	3242	505.5 (3.49 MPa)	5.2

flux) are studied, and scaling relations are obtained for transition times between dissolution regimes and for dissolution flux. Finally, we draw conclusions in Sec. IV, followed by Appendixes A–E that provide the details for the thermodynamic and physical properties of our fluid system.

II. METHODOLOGY

We conduct a series of eight experiments in high-pressure conditions at different medium permeabilities and salinity values. The details of the experiments conducted are given in Table II. To understand the effect of brine composition, we reduce the NaCl amount to 80% of its initial value, and for the remaining 20%, we add $CaCl_2$. For example, in the corresponding solution of 1 molal (m hereafter) NaCl, we use 0.8 m NaCl and 0.1 m $CaCl_2$. This way, there is a similar concentration of Cl^- in both solutions, and for each divalent cation of Ca^{2+}, there are two monovalent cations of Na^+ in the corresponding solution.

It is worth noting that the careful choice of salt types and their concentration is in accordance with the available literature data and the knowledge of field values (e.g., Refs. [65,67,68]).

Experiments are performed in a constant volume of a visual cell that we design. The cell has internal dimensions of $36 \times 30 \times 2.5 \, cm^3$ (internal volume of 2700 cm^3) with an aluminum frame covered with a 5-cm-thickness plexiglass enabling the visual examination (the setup is shown in Fig. 1). To prevent plexiglass expansion under high-pressure conditions, we attach a steel frame to the main frame. Here, the lower 23 cm of the cell is packed with glass beads. The glass bead size has a uniform distribution. We use a series of sieves to choose two size ranges of glass beads with 20–30 and 30–40 mesh size, resulting in 0.6–0.85-mm and 0.425–0.6-mm bead diameter sizes, respectively. With smaller glass beads, the quality of images would be compromised, whereas for larger glass beads, only very limited data are obtained for the early diffusion-dominated dissolution regime, rendering
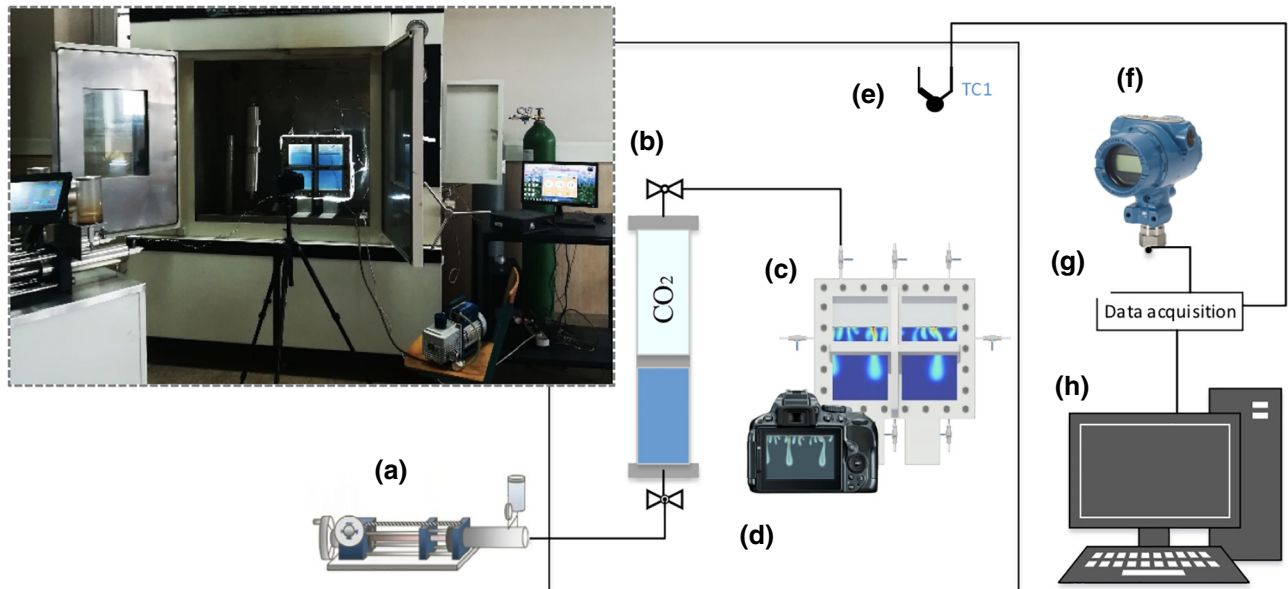

FIG. 1.   Experimental setup. (a) High-pressure pump, (b) pressure vessel cylinder, (c) visual cell, (d) digital camera, (e) thermocouple, (f) pressure gauge, (g) data acquisition system, and (h) a computer for data storage.

the calculation of diffusion coefficients inaccurate and the early transition times difficult to capture. The permeability range is 400–550 darcy and porosity is approximately 0.36 for all cases, determined by the selected glass bead size. We use a wider opening (2.5 cm) in our cell, which allows for adding such aporous structure into the cell, in a similar fashion to that of Liyanage *et al.* [69] and Newell *et al.* [23], as an improvement over previous Hele-Shaw or bulk-fluid experiments (e.g., Refs. [54,56]. For instance, the onset of convection in bulk-fluid experiments happens so instantaneously that usually there is not sufficient data in the early, diffusion-dominated regime. In the presence of a porous structure (a system with macroscale tortuosity and lower permeability and porosity than bulk fluid), conversely, we can obtain pressure data from the diffusion-dominated regime and hence calculate the diffusion coefficient from experimental data. Further, our new device has negligible boundary effects (with respect to both lateral and bounding walls) owing to its size; we observe no preferential flow at any cross sections of the cell (including those on or adjacent to the bounding plates). Given the above, our experiments cover a Ra range of 2919–4841, which is well within the expected values reported for various saline aquifers around the world [69].

In our experiments, the porous part of the cell is saturated with the desired brine solution; we introduce brine into the cell by continuous mixing and gradually adding NaCl or a mixture of NaCl and $CaCl_2$ into water. Bromocresol green is used as a pH indicator with a 0.02% weight fraction in brine. CO_2 is injected into the remaining 7 cm in the empty upper section—with no porous structure—to reach the desired pressure. This packing configuration helps to eliminate the capillarity effects as there is no longer a capillary transition zone between the initial brine- and CO_2-saturated layers. In practice, the cell is placed in an oven and a vacuum pump is used to saturate it with brine and the pH indicator solution. Then, the transfer vessel cylinder is loaded with the CO_2 gas phase. The CO_2-containing cell is pressurized, and all equipment in the oven is kept under $50\,^{\circ}C$ for at least 12 h. Our choice of temperature is well within the reported *in situ* values for geological target formations [20,70]. Before inserting gas into the cell, a pump vacuumizes the cell. A valve between the gas cylinder and the cell is opened gradually to reduce possible disturbances. Once we obtain a desired pressure, we close the cylinder valve and open the pressure gauge valve. Initial pressures for the tests are in the range of 502.6–535.3 psi (or approximately 3.47–3.69 MPa). The slight variation in these initial pressures is because the closing time of the cylinder valve is not exactly the same and the nonlinearity of the system in reaching the final equilibrium state follows that. Because our setup has a constant volume in the isothermal condition (approximately $50\,^{\circ}C$), the CO_2 dissolution into the brine results in some pressure reduction; the continuous

monitoring of this reduction from the sufficiently high initial pressures provides a reliable quantitative measure of dissolution. Pressure changes are therefore measured with a high-accuracy pressure gauge (±0.1-psi resolution). The pressure monitoring and the continuous capturing of visual snapshots with a digital camera are performed until the pressure reaches an almost constant value.

Following Wen *et al.* [43] and Slim *et al.* [39], we consider the domain height as an appropriate length scale for the long-term evolution of the convective system; we choose the diffusive nondimensional time, $t_D = tD/H^2$, as the characteristic time scale, where t, D, and H are the time, diffusion coefficient, and height of system, respectively. Based on this nondimensional time, we present an example picture of the dynamic evolution of pressure resulting from our experiments in Fig. 2.

As mentioned above, we calculate the diffusion coefficient values from the pressure data via the nonintrusive, fast pressure decay method [71] in the diffusion-dominated regime in our experiments and use these values in this study. By matching the experimental data with simple simulation models following our previous work [71,72], we are able to obtain diffusion coefficients. Unlike in previous experiments with blind cells where the gas-brine interface is unknown (e.g., Ref. [52]), the visual data from our experiments allow us to obtain the volume of the CO_2 gas phase (V). We perform image acquisition with a 3-min time frequency and analyze the images to obtain an accurate value for V. At each time instance, pressure is also recorded, though the frequency of pressure measurement is 5 s. Then, we use the following equation to calculate the amount of dissolved CO_2 in time [73]:

$$n_{\mathrm{diss},t}^{CO_2} = \left(\frac{PV}{zRT}\right)_i - \left(\frac{PV}{zRT}\right)_t, \qquad (4)$$

where $n_{\mathrm{diss},t}^{CO_2}$ shows the amount of dissolved CO_2 and i stands for the initial time condition. z is the compressibility
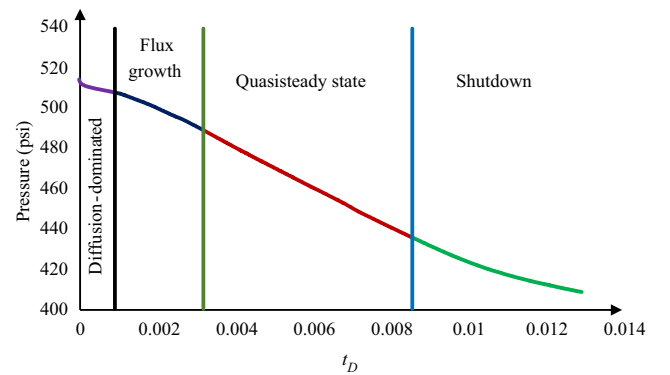

FIG. 2. Conceptual model for pressure reduction during the dissolution process. Different dissolution regimes are also shown and separated by vertical lines (these boundaries are obtained from a dissolution flux analysis).
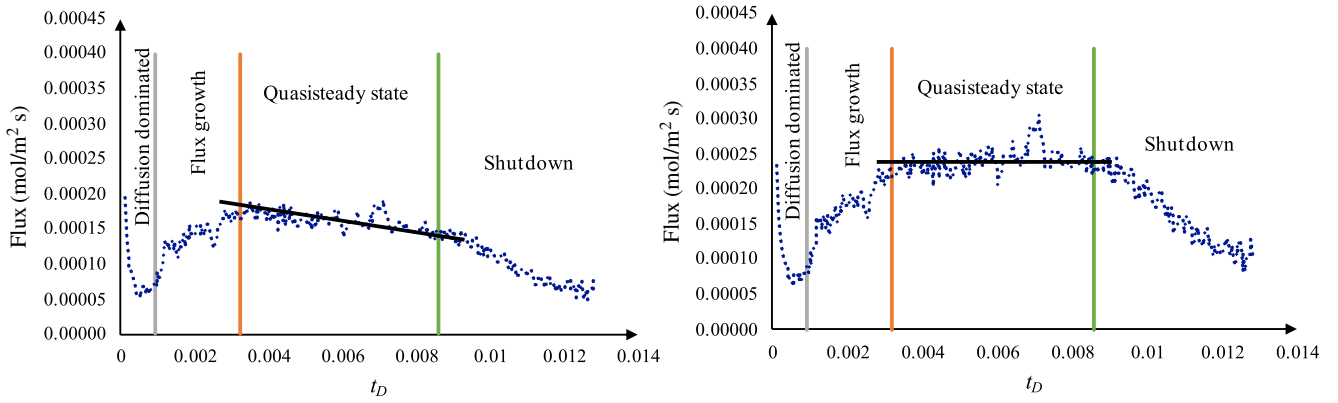
FIG. 3. Dissolution flux without modification for the closed system (left panel), and dissolution flux with our new compensation ($F_c/C_s^2 \times C_{s,0}^2 \approx F$) for the closed system (right panel).

factor obtained from the Peng and Robinson [74] equation of state in its polynomial form for capturing the possible deviations from ideal gas behavior. T is absolute temperature and R is the universal gas constant. The mole fraction of brine in the gas phase is assumed negligible (see Ref. [73]).

The accurate detection of different dissolution regimes is not feasible by pressure data only. Therefore, the dissolution flux F_c (mol/m^2 s) is used instead, which is calculated using the values of dissolved CO_2 in brine as follows:

$$\frac{dn_{\mathrm{diss}}^{\mathrm{CO_2}}}{dt} = AF_c, \qquad (5)$$

where A is the surface area of the gas-brine interface (here 0.025×0.36 m^2).

To detect the quasisteady regime in our closed system at the constant volume condition, we follow the analytical approach by Wen *et al.* [43], with the difference that we use $C_{s,0}^2$ (mol/m^3), the initial concentration of CO_2 at the interface, in our conversion to make it nondimensional as $F_c/C_s^2 \times C_{s,0}^2 \approx F$ (mol/m^2 s) for obtaining scaling relations. We discuss this modification later with details. Since the temperature and salinity are constant, the available correlations for the solubility of CO_2 in brine can be used to calculate the C_s values at any given pressure. Here, we use the solubility models by Duan and Sun [73] and Duan *et al.* [75] to calculate the CO_2 equilibrium concentration at the gas-brine interface. Importantly, these models show that an increase in salinity results in a reduction of solubility (i.e., equilibrium concentration).

Figure 3 shows the resulting dissolution flux for the presented pressure curve in Fig. 2. It should be noted that the fluctuating data of the dissolution flux are converted to produce a smooth curve via the moving average method. Based on the dissolution flux dynamics, the transition between dissolution regimes is detectable. The lines

illustrated in the figures show the onsets of convection, quasisteady, and shutdown regimes, respectively, from left to right.

While a pressure gauge with a high accuracy of approximately 0.1 psi is used in this study, pressure changes due to CO_2 dissolution over a small time period of the order of seconds are not detectable. We analyze the pressure data based on 8-min intervals.

III. RESULTS AND DISCUSSION

In this section, we present our results for the density-driven flow of CO_2 in brine solutions with dissolved NaCl and NaCl + CaCl$_2$. Specifically, we analyze the dissolution flux and the critical times for different flow regimes. Scaling relations are also presented. To verify the presented scaling relations against experimental observations, the individual transition times and dissolution rates are further compared with the predicted values.

A. Dynamics of dissolution

At early time, the dissolution of CO_2 into brine is a diffusion-dominated process. The mechanism behind the diffusive regime is well documented in the literature; the dissolution flux exhibits the classical Fickian scaling of $F \propto t^{-0.5}$ [18,26,27]. We present in Fig. 4 the visual results for our case 4 (introduced in Table II), where the brine has 1 M of NaCl and the permeability is 400 darcy. Figure 4(a) shows the first diffusive regime, where the diffusive layer can be seen as an almost pistonlike descending layer near the gas-brine interface.

The more dense CO_2-rich brine overlying the lighter fresh brine leads to a gravitationally unstable density stratification. Diffusion has a damping effect on these instabilities. As per Riaz *et al.* [37], in conditions with Ra greater than some critical values (e.g., Ra > 55) instabilities grow
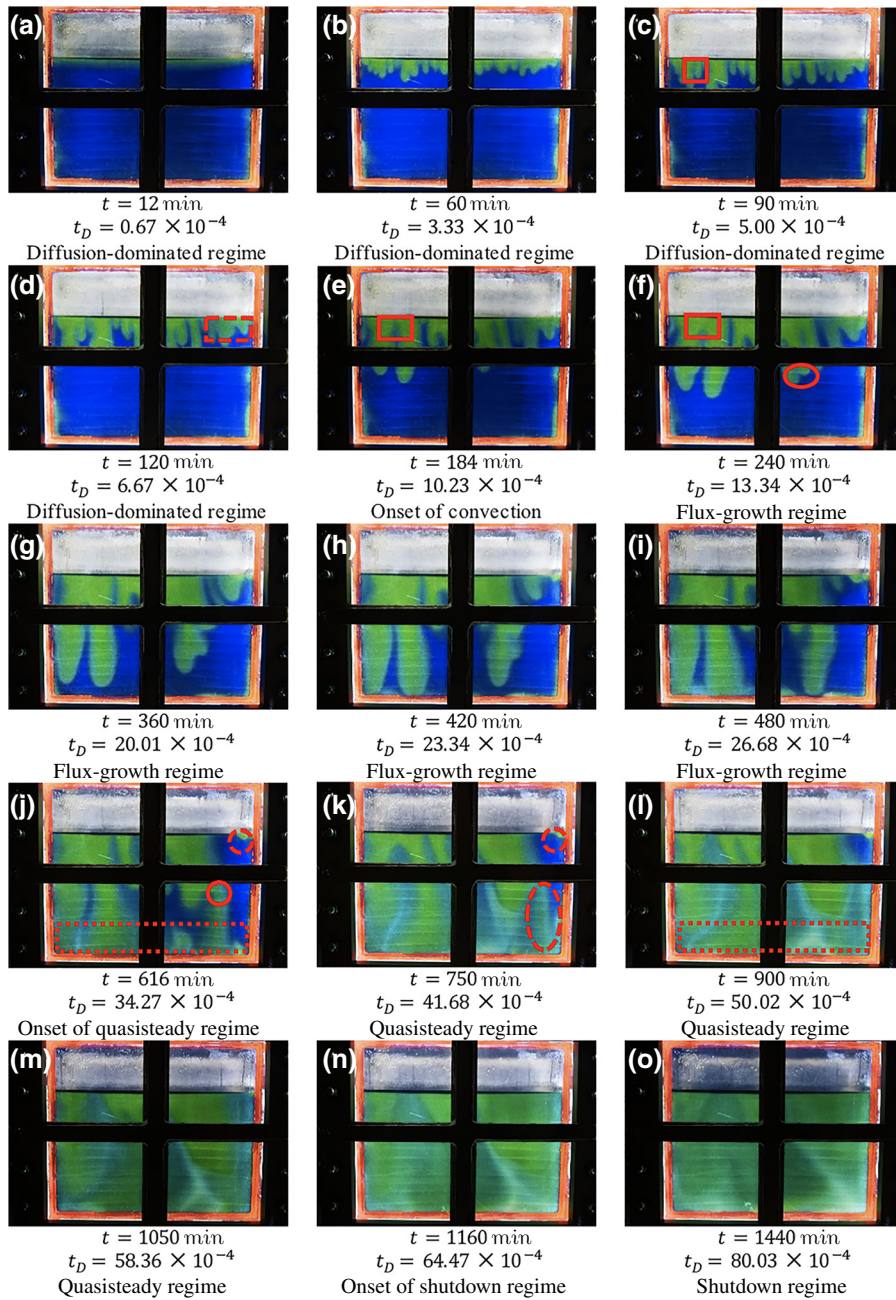
FIG. 4. The convection patterns for dissolved CO_2 in case 4; the green color shows the dissolved CO_2. Symbols are used to show the interactions of convective fingers as follows: square, side merging; dashed rectangle, fading fingers; rectangle, root zipping; oval, tip splitting; circle, necking; dashed circle, protoplume reinitiation; dashed oval, trailing lobe detachment.

(a) $t = 12\,\mathrm{min}$ $t_D = 0.67 \times 10^{-4}$ Diffusion-dominated regime

(b) $t = 60\,\mathrm{min}$ $t_D = 3.33 \times 10^{-4}$ Diffusion-dominated regime

(c) $t = 90\,\mathrm{min}$ $t_D = 5.00 \times 10^{-4}$ Diffusion-dominated regime

(d) $t = 120\,\mathrm{min}$ $t_D = 6.67 \times 10^{-4}$ Diffusion-dominated regime

(e) $t = 184\,\mathrm{min}$ $t_D = 10.23 \times 10^{-4}$ Onset of convection

(f) $t = 240\,\mathrm{min}$ $t_D = 13.34 \times 10^{-4}$ Flux-growth regime

(g) $t = 360\,\mathrm{min}$ $t_D = 20.01 \times 10^{-4}$ Flux-growth regime

(h) $t = 420\,\mathrm{min}$ $t_D = 23.34 \times 10^{-4}$ Flux-growth regime

(i) $t = 480\,\mathrm{min}$ $t_D = 26.68 \times 10^{-4}$ Flux-growth regime

(j) $t = 616\,\mathrm{min}$ $t_D = 34.27 \times 10^{-4}$ Onset of quasisteady regime

(k) $t = 750\,\mathrm{min}$ $t_D = 41.68 \times 10^{-4}$ Quasisteady regime

(l) $t = 900\,\mathrm{min}$ $t_D = 50.02 \times 10^{-4}$ Quasisteady regime

(m) $t = 1050\,\mathrm{min}$ $t_D = 58.36 \times 10^{-4}$ Quasisteady regime

(n) $t = 1160\,\mathrm{min}$ $t_D = 64.47 \times 10^{-4}$ Onset of shutdown regime

(o) $t = 1440\,\mathrm{min}$ $t_D = 80.03 \times 10^{-4}$ Shutdown regime

with time and result in the development of convective fingers [see Fig. 4(b)]. At this time, although the convective fingers are clear, their strength is not sufficient to make substantial changes to the pressure. At early times, convective fingers grow independently. As time passes and convective fingers grow enough, there are strong interactions between fingers.

The mechanisms that control the interactions between gravitational fingers are observed as follows.

(1) Side merging depicted by the square box in Fig. 4(c): The downward motion of a dominant finger and the upward migration of fresh brine from the bottom create a strong circulating velocity field toward the center of the finger, which in turn drives smaller fingers toward the dominant finger. Eventually, smaller fingers merge into the dominant finger, thus increasing its strength.

(2) Root zipping depicted by the (solid) rectangular box in Figs. 4(e) and 4(f): Two fingers merge from their roots.

(3) Tip splitting depicted by the oval in Fig. 4(f): The tip of a convective finger is flattened by the upward motion of brine and is likely to split into different portions.

(4) Necking depicted by the circle in Fig. 4(j): In some part of the finger, the width decreases and its feeding from the upper part decreases.

(5) Trailing lobe detachment depicted by the dashed oval in Fig. 4(k): A portion of the convective finger is separated from the root.
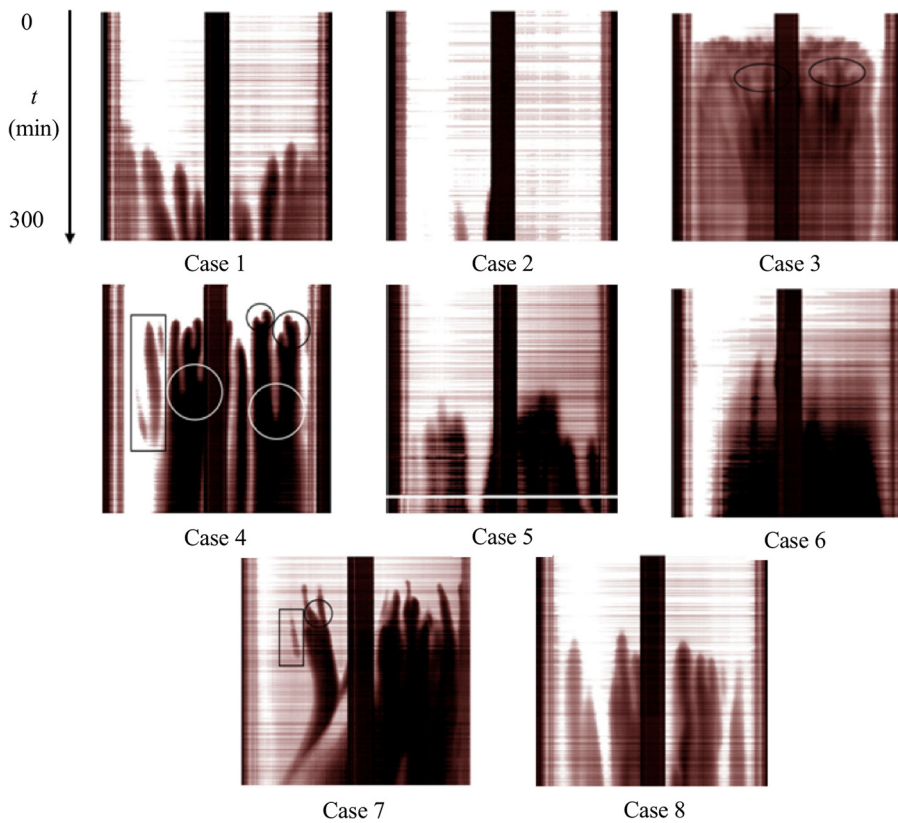
FIG. 5. Representative spatiotemporal diagrams of the dense fingers (shown by the darker intensity) at the depth of 5 cm below the gas-brine interface (the x axis is the width of cell at that depth, while the y axis is time). Symbols are used to show the behavior of convective fingers as follows: circle, the merging of convective fingers to make a stronger finger; rectangle, fingers that depart from the dominant finger and diffuse to the nearby stream; oval, the penetration of CO_2-enriched brine into the highly conductive conduits created by previous fingers. Note that the steel frame used to enhance the capability of the cell, particularly to tolerate the pressure, is seen with a thick black line in the middle of the pictures.

(6) Reinitiation depicted by dashed circles in Figs. 4(j) and 4(k): New small-scale fingers, known as protoplumes, are initiated between the dominant descending fingers in intermediate times during dissolution with the generation of concentration gradients below the interface due to the upwelling flow of fresh water.

(7) Fading fingers, partly clear in the dashed rectangle in Fig. 4(d): These fingers are created at early times and grow in a similar way as the surviving fingers. At some point, the growth of fading fingers cease, either when they intersect dominant plumes or through diffusive smearing, and they act as a sourcing pool for feeding the dominant fingers. Remarkably similar interactions have been reported in prior modeling work on viscous fingering and diffusive-convective dissolution [32,33,41,76–81].

Under the preceding mechanisms, the dominant convective fingers grow larger and stronger to reach a point at which the pressure decay data show a rapid decline (in comparison to the diffusion-dominated regime). This point is selected as the onset of convection, beyond which the pressure decreases at a greater rate in comparison to the diffusive regime. This time is an important factor from an operational standpoint since there is a pressure decline below the caprock, which implies a smaller magnitude of stress and thus a smaller risk of induced leakage. The FG regime follows the onset of convection, where the dominant fingers (or megaplumes) start to appear and then further develop, while enhancing the dissolution flux

across the formation via enhancing the concentration gradient at the gas-brine interface and around a stretching finger [82] [see Figs. 4(f)–4(i)].

To better elucidate the behavior of the convective fingers resulting in the flux enhancement, a narrow slice is selected at the depth of 5 cm below the gas-brine interface and the formation of dissolved CO_2 patterns over time is captured by representative spatiotemporal diagrams of the dense fingers (Fig. 5). Except for case 6, all cases follow a similar trend: the number of convective fingers and their speed increase with Ra. These characteristics (fingering number and their speed) are stronger for NaCl solutions in comparison to their corresponding $NaCl + CaCl_2$ mixtures. This is fundamentally because of the smaller diffusion coefficient for the former (NaCl) than the latter, which would result in larger Ra and thus more pronounced fingering (note that density difference and viscosity profiles for the corresponding brines of similar salinity are indeed similar to each other). The characteristic features of coarsening dynamics that have been identified in previous numerical studies and experiments on analog fluids are interestingly captured in our CO_2-brine experiments at high pressure as well. As an example, case 3 in Fig. 5 shows that when convective fingers sink down, they create low-resistance pathways where new high-concentration fluid preferentially follows the long-lived descending plumes toward the bottom of the system (signified by an oval-shaped symbol in the figure). As indicated by the circle symbols in case 4 of Fig. 5, the merging between fingers

is more predominant early on when small-scale instabilities emerge. Eventually, the continuous merging between neighboring plumes leads to the development of a few larger-scale coherent structures that serve as the conduits for traveling plumes. The rectangular boxes in cases 4 and 7 represent those weak convective fingers that fade while separating from a dominant one and diffusing into the main stream. It is encouraging to note that these observations from the interaction of the CO_2-saturated phase at relatively high pressure with the salt-containing aqueous phase within a porous medium are remarkably similar in nature to the predictions of previous studies that consider, both numerically and experimentally, the convection in a simplified one-phase system with no salinity or pressure effects.

Traditionally, when there is no gas cap and pressure change subject to dissolution, the flux grows to a maximum (owing to the mechanisms explained previously), beyond which merging and shielding between adjacent elongated fingers combined with diffusive spreading weaken the concentration gradients in the boundary layer. Hence, the dissolution flux stops growing and, in fact, it decreases transiently until a quasisteady constant-flux regime develops as a result of a balance between the reinitiation of protoplumes and the coarsening of the existing plumes followed by their subsumption [41]. Our experiments, however, reveal that such a quasisteady constant-flux regime actually never happens in a two-phase closed system, as suggested by Fig. 3. The pattern coarsening, as the mechanism for flux reduction, dominates the protoplume reinitiation that is the mechanism for flux enhancement [denoted by dashed circles in Figs. 4(j) and 4(k)]. This is because of the predominant decrease of pressure following the onset of convection, which in turn decreases the solubility of CO_2 in brine at the interface and, accordingly,

the dissolution-induced density change, i.e., the driving force for buoyancy-driven convection. The final outcome of this nonlinear dynamics is the decreasing trend, rather than a constant average value, of flux in the intermediate regime before the onset of final shutdown, as predicted theoretically by Wen *et al.* [43].

Despite the decreasing trend of flux in this regime, a quasisteady regime, however, is attainable in closed systems with the introduced compensation of dissolution flux as $F_c/C_s^2 \times C_{s,0}^2 \approx F$, as shown in Fig. 3. This is a modification to the scaling suggested by Wen *et al.* [43] as F_c/C_s^2. The results of experiments are analyzed based on the new correction to obtain transition times between dissolution regimes and the associated scaling relations.

Figure 6 shows the fingering patterns at the time of transition to the quasisteady regime for all cases. This regime persists until the upwelling flow starts to carry CO_2-rich fluid toward the gas-brine interface. Next, the concentration gradient at the interface and, consequently, the dissolution flux decay rapidly with time, resulting in the shutdown of the convective dissolution process. The transition to the convection shutdown regime is presented in Fig. 4(n), after which the position of megaplumes is almost constant and the region between adjacent megaplumes is slowly saturated, mainly by the diffusion mechanism [Fig. 4(o)].

Our findings suggest that the onset of the shutdown regime occurs after twice the time required for the first fingers to reach the bottom. The results show that the first contact, e.g., for case 4, occurs at almost 480 min after the start of the experiment [Fig. 4(h)], but the shutdown regime starts at approximately $1160 > 2 \times 480$ min. Further analysis of the visual data explains this behavior. As displayed in Figs. 4(j) and 4(l) with the dashed rectangular boxes, when the convective fingers reach the impermeable
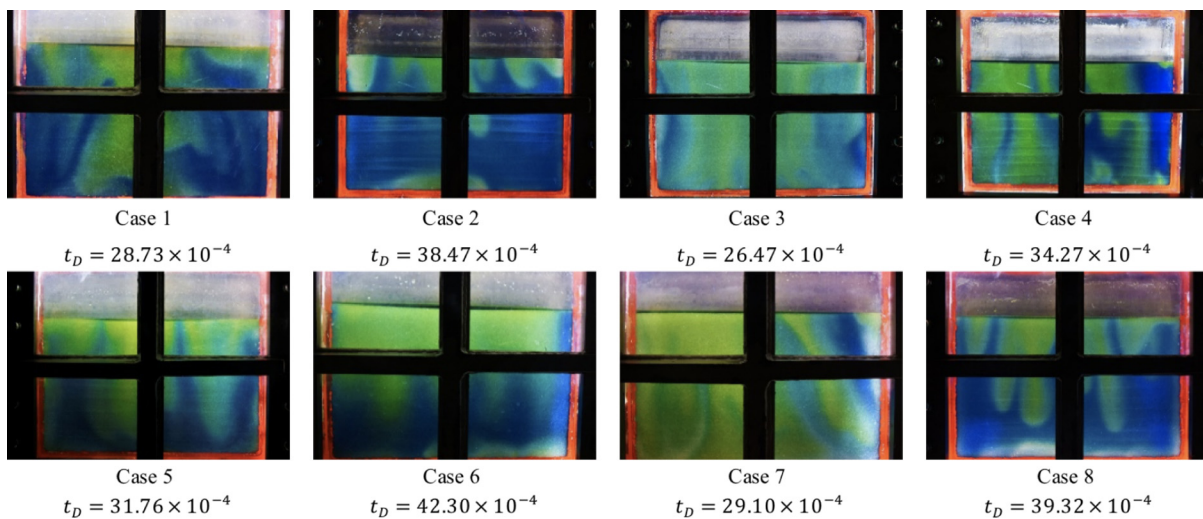

FIG. 6. Convective fingers at transition times to the quasisteady regime. Different Ra values of these cases result in a different transition time to the intermediate quasisteady regime.

bottom of the system, they initially propagate laterally therein before rising upward with the upwelling flow. The traveling speed of a rising plume following an impact with the bottom boundary is slower than that of the sinking plumes, partly due to a greater lateral extent (surface area) for the rising fluid (i.e., a mixture of brine and dissolved CO_2) as compared to each sinking finger. Therefore, the onset time of the shutdown regime is greater than twice the time required for the first impact with the bottom boundary. Note that blind-cell experiments could not observe this. It should also be noted that the transition times between dissolution regimes are obtained here through quantitative data and are discussed subsequently with details.

B. Scaling analyses

Pressure data obtained from our tests are presented in Fig. 7. During the diffusion-dominated regime, pressure (besides temperature) is almost equal for all cases. Therefore, salinity controls the diffusion coefficient and, consequently, the dissolution rate during the first diffusion-dominated regime (see Table II). $NaCl + CaCl_2$-containing brines show a slightly higher diffusion coefficient than the corresponding NaCl brines, most likely due to the lower total molality for the NaCl and $CaCl_2$ mixture as well as the different molecular interactions in different salt solutions (see Table II). In light of this observation, the dissolution rate for $NaCl + CaCl_2$ brine is higher in the first diffusion-dominated regime. The increase in salinity results in the reduction of the diffusion coefficient (as also recently shown and explained elsewhere [83]), which leads to the lower dissolution rates in the diffusion-dominated regime, and thus lower pressure decline, for cases with higher salinity (Fig. 7).

To obtain scaling relations for the dissolution flux and the transition times between dissolution regimes, we convert the pressure data to dissolution flux with the help of visual data for the dynamic volume of the gas phase. We calculate the modified dissolution flux based on Eq. (3) [43] for the quasisteady regime to investigate
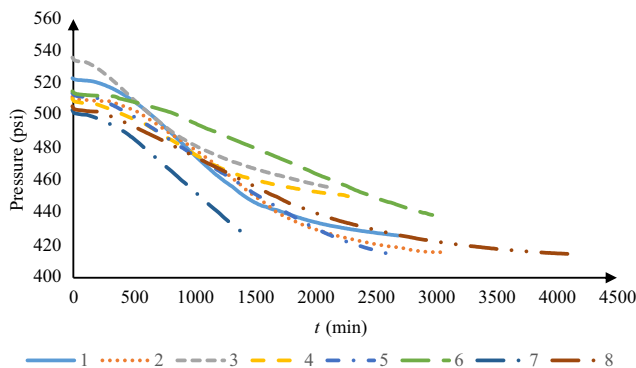

FIG. 7. Pressure data obtained from experimental tests.

TABLE III. Detailed information for the scaling of dissolution flux in the (time-dependent) FG regime [Eq. (6)], in the (time-independent) quasisteady regime [Eq. (11)], and also in the (time-dependent) shutdown regime (i.e., $F = a^{sd} t_D^{-2}$), as well as the onset times for the quasisteady regime [Eqs. (9) and (10)], and finally the onset time for the final shutdown regime [Eqs. (12) and (13)], all for each case directly from (or fitted to) experimental measurements (denoted by subscript fit), as well as from the reported global scaling relations (denoted by subscript est).

Case	F_c/C_s^2	$m_{fit}^{FG} \times 10^4$	$b_{fit}^{FG} \times 10^6$	$m_{est}^{FG} \times 10^4$	$b_{est}^{FG} \times 10^6$	$t_{D,fit}^{QS} \times 10^4$	$t_{D,est}^{QS} \times 10^4$	$a_{fit}^{QS} \times 10^4$	$a_{est}^{QS} \times 10^4$	$t_{D,fit}^{SD} \times 10^4$	$t_{D,est}^{SD} \times 10^4$	$a_{fit}^{SD} \times 10^9$
1	7	77	−124	78	−134	28.73	28.58	2.90	2.95	54.13	53.03	8.3
2	5	45	−52	43	−50	38.47	37.64	2.20	2.09	71.00	70.47	11
3	4.1	96	−173	90	−162	26.47	26.46	3.30	3.24	48.10	48.99	6.5
4	3.4	55	−65	50	−68	34.27	35.30	2.30	2.26	64.47	65.95	5.5
5	4.5	61	−92	62	−95	31.76	32.14	2.40	2.54	85.76	85.88	18.0
6	3.8	31	−31	32	−25	42.30	42.99	1.70	1.84	104.9	105.18	18.2
7	4.6	64	−121	73	−123	29.10	29.19	2.80	2.83	80.31	80.30	17
8	3.2	42	−46	42	−48	39.32	38.67	2.20	2.07	98.14	97.69	15.6

the possible scaling relations with this character. Note that such a modified dissolution flux in the quasisteady regime is independent of time. Results are reported in Table III.

We find that F_c/C_s^2 surprisingly does not show any specific trend with Ra (Tables II and III); this will still happen if we alternatively rescale for all cases the C_s with only a single concentration value, e.g., from any of the initial conditions. To better understand the reason behind this, let us consider two situations: (i) Ra is increased through an increase in permeability (e.g., case 1 versus case 2). In this situation, the dissolution flux (F_c) increases with Ra at a given time, while there are no considerable changes in the CO2 solubility values (C_s); therefore, the overall value of F_c/C_s^2 is found to increase with Ra in this situation (e.g., from 5 in case 2 to 7 in case 1). (ii) Ra is increased through a reduction in salinity (e.g., case 1 versus case 3). Whereas the F_c increases in this situation, the C_s increases as well (see Sec. II), and the overall value of F_c/C_s^2 actually decreases (from 7 in case 1 to 4.1 in case 3). Based on this explanation and opposing situations, we find that *how* Ra changes specifically (via salinity or permeability) is important for the dynamical behavior of F_c/C_s^2, and there is not a general relation between the latter and Ra.

Given the definition of the Sherwood number as $\mathrm{Sh} = F_c/D\varphi\Delta C/H = F_c/D\varphi c_{b,\mathrm{max}}^s x_{\mathrm{CO_2,max}}^s/H$ [41], Sh values show a decreasing trend during the quasisteady regime in a closed system. This is indeed because of the decreasing dynamics of F_c in this regime as shown previously and the other parameters assumed as constant (see Fig. 3). Further, $c_{b,\mathrm{max}}^s$ (constant maximum density of brine) and $x_{\mathrm{CO_2,max}}^s$ (constant maximum solubility fraction) in the formulation of Sh do change with salinity and, thus, the problem mentioned previously with F_c/C_s^2 scaling with Ra applies to Sh scaling as well.

To overcome these physical challenges in obtaining rigorous scaling relations, we propose a further adjustment as $F_c/C_s^2 \times C_{s,0}^2 \approx F$, where $C_{s,0}^2$ is the initial concentration of CO2 at interface and itself sensitive to salinity, such that the dynamic changes in C_s^2 are compensated with $C_{s,0}^2$. The results are presented in Fig. 8 for all cases.

The analysis of dissolution flux dynamics shows that for the solutions of both NaCl and NaCl + CaCl2, the dissolution flux increases with time as $t_D^{0.5}$ in the FG regime. This is consistent with the findings of Newell *et al.* [23]. Higher Rayleigh numbers result in a greater number of convective fingers with more strength. Therefore, we hypothesize that the dissolution flux at a given equal time in the FG regime should be greater than that for a lower Ra case; i.e., the prefactor for the $t_D^{0.5}$ scaling should be positively correlated with Ra. Furthermore, as shown in Fig. 5 and in supplementary videos (Videos 1 and 2), the number of convective fingers and their strength (quantified with sinking speed) are higher for brine with NaCl than for brine with NaCl + CaCl2 mixtures. Dissolution flux data can quantify these observations. The relation with the following formula is used to fit the dissolution flux data (with continuous curve):

$$F = m^{\mathrm{FG}} t_D^{0.5} - b. \qquad (6)$$

Values of the m^{FG} and b are reported for each experiment, denoted by $m_{\mathrm{fit}}^{\mathrm{FG}}$ and $b_{\mathrm{fit}}^{\mathrm{FG}}$ in Table III. Detailed analysis of these factors proves that they interestingly scale linearly with Ra, as follows

$$m^{\mathrm{FG}} = (2.99 \times 10^{-6}) \,\mathrm{Ra} - 5.48 \times 10^{-3}, \qquad (7)$$

$$b = (-7.1 \times 10^{-8}) \,\mathrm{Ra} + 1.83 \times 10^{-4}. \qquad (8)$$

The estimated values based on these equations are further reported in Table III as $m_{\mathrm{est}}^{\mathrm{FG}}$ and $b_{\mathrm{est}}^{\mathrm{FG}}$. The modified dissolution flux continues to increase until it plateaus in the quasisteady period. This time is detected as the onset of quasisteady regime ($t_{D,\mathrm{fit}}^{\mathrm{QS}}$) and is reported in Table III. Results reveal that this onset occurs earlier for cases with higher Ra in both mixture types. This is because the interactions between convective fingers are more intense at higher Ra and, therefore, the megaplumes form earlier during the experiments. Based on the same reasoning, NaCl solutions show an earlier onset for the quasisteady regime in comparison with their corresponding NaCl + CaCl2 solutions. Detailed analysis of the onset of the quasisteady regime shows that they correlate through the following equations with Ra in two mixtures:

$$t_{D,\mathrm{NaCl}}^{\mathrm{QS}} = 5.437 \times \mathrm{Ra}^{-0.899}, \qquad (9)$$

$$t_{D,\mathrm{NaCl+CaCl_2}}^{\mathrm{QS}} = 13.591 \times \mathrm{Ra}^{-1.01}. \qquad (10)$$

Estimated times for the onset of the quasisteady regime ($t_{D,\mathrm{est}}^{\mathrm{QS}}$) with the proposed scaling relations are presented in Table III and show good agreement with the fitted values. As discussed in Fig. 4, protoplume reinitiation helps to maintain the dissolution flux during the quasisteady regime. Cases with higher Ra show a higher (modified) dissolution flux during this regime. These constant dissolution rates (which are presented with $a_{\mathrm{fit}}^{\mathrm{QS}}$) are best fitted with Eq. (11) for all cases with a coefficient of determination (R^2) of 0.944, as follows

$$F = a^{\mathrm{QS}} = (2.30 \times 10^{-8}) \,\mathrm{Ra}^{1.126}, \qquad (11)$$

the resulting estimations are reported with the symbol of $a_{\mathrm{est}}^{\mathrm{QS}}$. The almost linear scaling of the compensated dissolution flux with Ra obtained from our experiments is somewhat striking given the debate that exists for the flux scaling (linear versus sublinear) in the quasisteady regime (see Table I). Note that the Rayleigh number carries the majority of the information of a formation at a
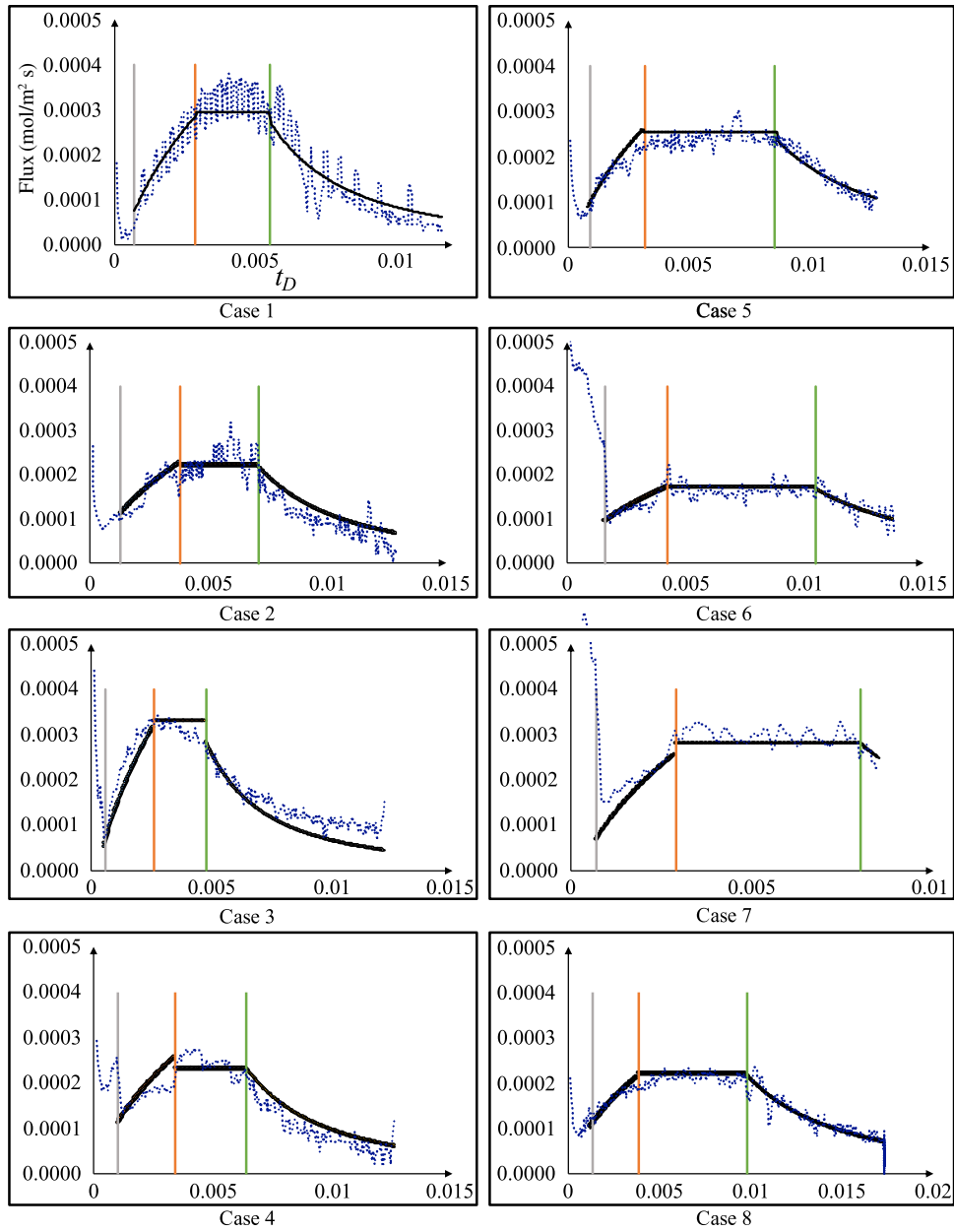
FIG. 8. Compensated dissolution flux ($F_c/C_s^2 \times C_{s,0}^2 \approx F$ with dotted line) and fitting curves (continuous line) versus dimensionless times for our experiments, which clearly distinguish the quasisteady regime from early FG and final shutdown regimes.

given pressure, temperature, salinity, height, permeability, and porosity. As a result, a scaling relation obtained based on Ra is not only irrespective of its original experimental conditions, but it is also, in practice, applicable to other reservoir conditions. In our experiments, with the new two-phase CO_2-brine system, only a sufficiently high initial pressure is desired in order for (i) CO_2 to diffuse into the underlying brine at a fast enough rate and for (ii) a much more accurate measurement of diffusion coefficients in the early stage as well as the dissolution flux afterward from the pressure drop that arises during the dissolution process (as previously explained). Moreover, motivated by

previous scaling relations summarized in Table I, we also report on the scaling of the Sherwood number versus Ra as well. Based on the rescaled dissolution flux, we interestingly find two power-law relations that best fit the data for the quasisteady regime. Our scaling analyses reveal a best-fit power law of $Sh = 1.238Ra^{0.981}$ with an R^2 of 0.984 for the 1M brine and $Sh = 0.332Ra^{1.183}$ with an R^2 of 0.82 for the 2M brine solutions. This distinction is due to the reduction of solubility at higher salinities [73,75], leading to a relatively smaller scale for the purely diffusive flux [Eq. (2)] and hence an upward shifting of the Sherwood number in higher salinities.
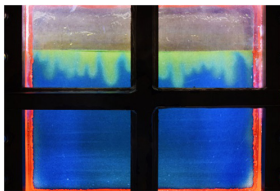
VIDEO 1. CO_2 dissolution dynamics for case 4.

The dissolution process continues in the quasisteady regime until the wavefront of CO_2-rich brine from the bottom reaches the interface. It is expected to find an earlier onset of the shutdown regime for higher Ra cases just because of its control on the traveling speed of convective fingers. We observe that our experimental results meet this expectation. Another key feature we find is that $NaCl + CaCl_2$ solutions show longer duration of the quasisteady regime as compared to the corresponding NaCl solutions (Fig. 8). This can be justified by our previous explanation as to why the onset of shutdown takes more than two times the time of the first impact with the bottom boundary; lower Ra for the $NaCl + CaCl_2$ solutions compared to their corresponding NaCl brine would result in even longer travel times for the rising wavefront. Hence, the onset of shutdown occurs much later for $NaCl + CaCl_2$ than for an equivalent NaCl solution, accordingly with the longer duration of the quasisteady regime. The analysis of the onset of shutdown times ($t_{D,\text{fit}}^{\text{SD}}$) shows that the following relations describe the transition times well, as follows

$$t_{D,\text{NaCl}}^{\text{SD}} = 12.874 \times \text{Ra}^{-0.928}, \quad (12)$$

$$t_{D,\text{NaCl}+\text{CaCl}_2}^{\text{SD}} = 18.659 \times \text{Ra}^{-0.929}. \quad (13)$$

The corresponding estimated values ($t_{D,\text{est}}^{\text{SD}}$) with these relations are reported in Table III and show close agreement with the fitted values. During the shutdown regime, the CO_2 concentration gradient at the gas-brine interface constantly decreases while reducing the dissolution flux. Whereas the previous theoretical and numerical studies reported a $F \propto t^{-2}$ characteristic behavior during this regime [40,42,43], recent experiments of Newell *et al.* [23] suggested a $F \propto t^{-1.75}$ scaling during the shutdown regime. Our experiments remarkably confirm the temporal scaling behavior of the theoretical and numerical studies, where $F = a^{\text{SD}} t_D^{-2}$ describes our results (see the

VIDEO 2. CO_2 dissolution dynamics for case 8.

continuous line during this regime in Fig. 8). Prefactors of a^{SD} are also reported in Table III. These values, however, do not show a distinct trend with Ra. It seems that they are a function of diffusion coefficients and depend on the history of prior regimes. Cases with higher salinity show larger values for the prefactor, because of their lower concentration of dissolved CO_2 as a result of prior dissolution events. The $NaCl + CaCl_2$ mixtures show higher prefactors in comparison to their corresponding NaCl solutions because of larger diffusion coefficients.

IV. DISCUSSION AND CONCLUSIONS

In this study, high-pressure laboratory experiments are performed to examine the convective dissolution of actual CO_2 in a closed porous media system saturated with brines that contain NaCl and $NaCl + CaCl_2$ mixtures at different molality. The common concerns of previous studies that use analog fluid systems to emulate the CO_2-brine behavior, such as the nonmonotonic density profile and miscibility of the system, are resolved in our work. Further, in comparison to the experiments performed in blind cells, visual data are available in this study, enabling us to examine the dynamics of convective fingers during dissolution. Performing the experiments at high pressure not only more closely reflects the subsurface conditions but also makes it possible to obtain diffusion coefficients and dissolution fluxes through the measurable pressure changes during the dissolution process. Our alternative engineering design provides an unprecedented opportunity to bridge the gaps among the visual low-pressure Hele-Shaw and high-pressure blind cell experiments as well as those with analog fluids. Juxtaposing the qualitative and quantitative data in this study further decreases the possible errors during data analysis.

Qualitative data (image) analyses reveal that, at early times, the dissolution process is diffusion dominated. The dissolution of CO_2 into underlying brine creates a flat diffusive boundary layer under the gas-brine interface. The mixture of CO_2 and brine overlying the lower density fresh brine leads to a gravitationally unstable stratification. When the diffusive boundary layer is thickened enough, instabilities initiate and grow as convective fingers. Following their appearance, convective fingers grow independently, early on, but as time goes on they interact more with each other and create stronger fingers. Seven mechanisms for fingering interactions are identified in this study as follows: side merging, root zipping, tip splitting, necking, trailing lobe detachment, protoplume reinitiation, and fading fingers. We find that the number of convective fingers, their speed, and their interactions are higher in NaCl solutions as compared to the corresponding $NaCl + CaCl_2$ solutions. In each type of solution, the speed of fingers and their interactions are positively correlated with Ra. Increasing salinity results in a decrease of convective flow

strength. After some period of time, convective fingers develop into larger-scale coherent structures and the quasisteady regime starts, at which time new smaller-scale fingers emerge at the gas-brine interface, helping the maintenance of dissolution flux. However, the considerable reduction in gas pressure following CO_2 dissolution, especially after the onset of convection, results in a reduction in solubility and concentration at the gas-brine interface. The flux-enhancing protoplume reinitiation is thus reduced, such that it is no longer sufficient to balance the flux-reducing coarsening mechanisms. The final outcome is a progressively decreasing trend in flux within the intermediate regime before the onset of the shutdown regime. The latter begins when the brine brought to the interface starts to contain dissolved CO_2 at late times, following which the position of megaplumes is almost constant and the region in between is slowly saturated mainly through diffusion. The onset of the shutdown regime occurs earlier for NaCl solutions.

Our experiments are conducted in a constant volume condition. Consequently, the dissolution of CO_2 into brine is accompanied by a reduction of the pressure of the gas phase. The analysis of pressure data provides a unique quantitative measure of the dynamic process. In previously reported experiments in high-pressure blind cells, the pressure is either maintained in the entire system and, hence, the dissolution flux behaves differently as compared to that in a confined medium [23,24] or it drops continuously [52,55], despite which the volume of the gas phase is assumed constant due to the lack of visual information. As a result, there has been a lack of robust scaling relations and interpretations of different events so far for the more complex two-phase convective systems, especially in the intermediate, quasisteady regime. Here, to detect the transition between dissolution regimes and reveal the scaling behavior of dissolution, the dissolution fluxes are calculated from the pressure curves with the help of visual data for gas volume. Further, we introduce a modification to the dissolution flux in order to yield insights into the scaling of the quasisteady regime (similar to open systems) as a function of Ra. With the conversion of $F_c/C_s^2 \times C_{s,0}^2 \approx F$, dissolution fluxes in the closed system appear to become constant during the quasisteady regime. Using this definition of flux, four dissolution regimes are identified as follows: diffusion-dominated; FG; quasisteady, and shutdown regimes. Scaling relations based on the dimensionless numbers are introduced for the transition times between these regimes. All transition times for the quasisteady and shutdown regimes for different salt types exhibit an inverse proportionality with Ra. However, the comparison between results reveals that NaCl solutions show earlier onsets of quasisteady and shutdown regimes as compared with those from the corresponding $NaCl + CaCl_2$ solutions. The difference between the onset times of shutdown in the two types of brine is larger than

those of the quasisteady regime. Therefore, $NaCl + CaCl_2$ systems experience a longer period in the quasisteady regime. The dissolution flux in all cases follows the $F \propto t_D^{0.5}$ and $F \propto t_D^{-2}$ scaling behavior for the FG and shutdown regimes, respectively. During the FG regime, the prefactors for $F \propto t_D^{0.5}$ for NaCl solutions are higher than those for $NaCl + CaCl_2$ solutions, and both linearly scale with Ra. Further, NaCl solutions show higher dissolution fluxes than $NaCl + CaCl_2$ mixtures during the quasisteady regime, with the compensated dissolution fluxes almost linearly scaling with Ra irrespective of salt types. For the shutdown regime, the dissolution rates for $NaCl + CaCl_2$ mixtures are also higher.

For carbon capture and storage applications and various potential geological sites, we can use the obtained scaling relations to estimate the relevant time scale for faster, convective dissolution of CO_2 and the scale of the dissolved amount relative to those for an otherwise purely diffusive process. The Bravo Dome CO_2 field in New Mexico has been recently shown to comprise a number of isolated pressure compartments resulting in confined systems of CO_2 gas and the underlying aqueous layer [57]. However, this field has been reported with an estimated initial Ra ≈ 540 [43], which is not only below the range studied here but may also be insufficient for a well-developed quasisteady convection regime, as suggested by Wen *et al.* [43]. In light of this, we consider a (hypothetically closed) saline formation in previously reported region b of the Mt. Simon sandstone [70]. Based on the available data set, $k = 9.87 \times 10^{-14}$ m^2, $\Delta\rho = 8$ kg/m^3, $g = 9.81$ m/s^2, $H = 200$ m, $\mu = 10^{-3}$ Pa s, $\phi = 0.2$, and $D = 1.97 \times 10^{-9}$ m^2/s (after Ref. [84]), which together result in Ra ≈ 3930. We consider two scenarios for this field: (1) brine salinity is composed of 100% NaCl and (2) brine salinity is composed of 80% NaCl and 20% CaCl$_2$. The characteristic diffusive time scale ($\sim H^2/D$) is about 644,000 years, i.e., the approximate time required for CO_2 to saturate the entire formation through diffusion alone. Our experimental findings [85] predict that sets in after 570 years. The onset of a well-developed quasisteady regime occurs around 2054 and 2049 years for the first and second scenarios, and the final shutdown regime starts in 3827 and 5501 years, respectively. These show that the time to convectively—as opposed to diffusively—mix CO_2 is significantly shortened. The stabilized compensated dissolution flux during the quasisteady regime is also approximately equals 8100 mol/(m^2 yr), which can translate to a significant maximum dissolution rate given the typically large areal extent of CO_2 plumes [46]. Note that the latter magnitude is the actual flux F_c rescaled by $(C_s/C_{s,0})^2$. The F_c changes continuously with time and pressure in such closed systems. Hence, the knowledge of pressure and solubility in time (e.g., via the correlation in Appendix A) is required if one is interested in knowing the total amount of dissolved CO_2 by a certain time, though knowing only

the initial solubility could still yield an upper bound on the dissolution amount.

Findings of this study advance our knowledge of CO_2 dissolution into formation brine following geological sequestration in deep saline aquifers. Scaling relations are introduced based on the dimensionless numbers, which enable us to use them in similar studies and possibly field experiments. Since $CaCl_2$ is the most common salt after NaCl in the majority of aquifers, this work helps to obtain a more realistic estimation for the short- and long-term fate and transport of CO_2—particularly in terms of the dissolution flux and transition times between critical regimes—following its storage in the subsurface.

APPENDIX A: SOLUBILITY OF CO_2 IN BRINE

Solubility of CO_2 in brine can be obtained from Duan and Sun [73] and Duan *et al.* [75]:

$$
\begin{aligned}
\ln x_{CO_2} = {} & \ln \left(y_{CO_2} \phi_{CO_2} P \right) - \frac{\mu_{CO_2}^{1(0)}}{RT} - 2\lambda_{CO_2\text{-Na}} \\
& \times \left(m_{Na} + m_K + 2m_{Ca} + 2m_{Mg} \right) \\
& - \zeta_{CO_2\text{-Na-Cl}} m_{Cl} \left(m_{Na} + m_K + m_{Mg} + m_{Ca} \right) \\
& + 0.07 m_{SO4},
\end{aligned} \tag{A1}
$$

where T is given in kelvins and pressure in bars. $\mu_{CO_2}^{1(0)}$, $\lambda_{CO_2\text{-Na}}$, and $\zeta_{CO_2\text{-Na-Cl}} m_{Cl}$ are the standard chemical potential; interaction parameter between CO_2 and Na^+; and interaction parameter among CO_2, Na^+, and Cl^- respectively. The following expression is used to calculate these parameters:

$$
\begin{aligned}
\text{Par}(T, P) = {} & c_1 + c_2 T + \frac{c_3}{T} + c_4 T^2 + \frac{c_5}{(630 - T)} \\
& + c_6 P + c_7 P \ln T + c_8 \frac{P}{T} + c_9 \frac{P}{(630 - T)} \\
& + c_{10} \frac{P^2}{(630 - T)^2} + c_{11} T \ln P.
\end{aligned} \tag{A2}
$$

The fugacity coefficient (ϕ_{CO_2}) is calculated from the following noniterative equation:

$$
\begin{aligned}
\phi_{CO_2} = {} & c_1 + \left(c_2 + c_3 T + \frac{c_4}{T} + \frac{c_5}{T - 150} \right) P \\
& + \left(c_6 + c_7 T + \frac{c_8}{T} \right) P^2 + \frac{\left(c_9 + c_{10} T + \frac{c_{11}}{T} \right)}{\ln P}.
\end{aligned} \tag{A3}
$$

Constants of c_1–c_{11} with respect to each of the above-mentioned parameters are presented in Table IV.

APPENDIX B: VISCOSITY OF NACL SOLUTION

Viscosity of NaCl solution can be obtained from Mao and Duan [86], as follows:

$$
\ln \left(\frac{\mu_{\text{brine of }CO_2}}{\mu_{H_2O}} \right) = Am + Bm^2 + Cm^3, \tag{B1}
$$

where A, B, and C are functions of temperature (in kelvins):

$$
A = c_1 + c_2 T + c_3 T^2, \tag{B2}
$$

$$
B = c_4 + c_5 T + c_6 T^2, \tag{B3}
$$

$$
C = c_7 + c_8 T. \tag{B4}
$$

c_1–c_8 are obtained from the experimental data and available in Table V.

APPENDIX C: VISCOSITY OF CACL$_2$ + NACL SOLUTION

To obtain the viscosity of the $NaCl + CaCl_2$ solution, the simple mixing rule is used [87]:

$$
\Delta \mu_{\text{mix}} = \Delta \mu_{CaCl_2} + \Delta \mu_{NaCl}, \tag{C1}
$$

TABLE IV. Parameters of c_1–c_{11}, required in CO_2 solubility equations.

Constant	$\mu_{CO_2}^{1(0)}/RT$	$\lambda_{CO_2\text{-Na}}$	$\zeta_{CO_2\text{-Na-Cl}} m_{Cl}$	ϕ_{CO_2}
c_1	28.9447706	-0.411370585	$3.36389723 \times 10^{-4}$	1.0
c_2	-0.0354581768	$6.07632013 \times 10^{-4}$	$-1.98298980 \times 10^{-5}$	4.7586835×10^{-3}
c_3	-4770.67077	97.5347708	...	$-3.3569963 \times 10^{-6}$
c_4	$1.02782768 \times 10^{-5}$	...	...	0.0
c_5	33.8126098	...	...	-1.3179396
c_6	$9.04037140 \times 10^{-3}$	...	...	$-3.8389101 \times 10^{-6}$
c_7	$-1.14934031 \times 10^{-3}$	...	...	0.0
c_8	-0.307405726	-0.0237622469	$2.12220830 \times 10^{-3}$	2.2815104×10^{-3}
c_9	-0.0907301486	0.0170656236	$-5.24873303 \times 10^{-3}$	0.0
c_{10}	$9.32713393 \times 10^{-4}$	...	...	0.0
c_{11}	...	$1.41335834 \times 10^{-5}$	...	0.0

TABLE V.   Required parameters for the viscosity models.

Constant	Mao and Duan's model [86]	Zhang et al. model [87]
c_1	-0.21319213	0.0061
c_2	$0.13651589 \times 10^{-2}$	...
c_3	$-0.12191756 \times 10^{-5}$	0.01040
c_4	$0.69161945 \times 10^{-1}$	0.000756
c_5	$-0.27292263 \times 10^{-3}$	...
c_6	$0.20852448 \times 10^{-6}$	0.0157
c_7	$-0.25988855 \times 10^{-2}$	0.271
c_8	$0.77989227 \times 10^{-5}$	0.04712
c_9	...	0.00941
c_{10}	...	0.00003

$$\mu_{mix} = \mu_{H_2O} \left(1 + \Delta\mu_{mix}\right), \tag{C2}$$

$$\Delta\mu_{NaCl} = c_1 m_{NaCl}^{0.5} + c_2 m_{NaCl} + c_3 m_{NaCl}^2$$
$$+ c_4 m_{NaCl}^{3.5} + c_5 m_{NaCl}^7, \tag{C3}$$

$$\Delta\mu_{CaCl_2} = c_6 m_{CaCl_2}^{0.5} + c_7 m_{CaCl_2} + c_8 m_{CaCl_2}^2$$
$$+ c_9 m_{CaCl_2}^{3.5} + c_{10} m_{CaCl_2}^7, \tag{C4}$$

where c_1–c_{10} are calculated from the experimental data on the specific concentration of the salts. In the required concentrations, parameters are interpolated. For a $1M$ concentration of brine, these values are presented in Table V.

APPENDIX D: BRINE DENSITY

The NaCl solution density is given as [88]

$$\rho_b = \frac{1000\rho_w + M_{NaCl}m_{NaCl}\rho_w}{1000 + A_0 m_{NaCl}\rho_w + B_0 m_{NaCl}^{1.5}\rho_w + C_0 m_{NaCl}^2\rho_w}. \tag{D1}$$

To obtain the NaCl + CaCl$_2$ solution density, the relative density of the NaCl + CaCl$_2$ mixture to the NaCl solution is calculated by the Al Ghafri et al. model [89]:

$$\rho_b(T, P, m) = \rho_{ref}(T, m)$$
$$\times \left[1 - C(m)\ln\left(\frac{B(T,m) + P}{B(T,m) + P_{ref}(T)}\right)\right]^{-1}, \tag{D2}$$

$$\ln\frac{P_{ref}(T)}{P_c} = \left(\frac{T_c}{T}\right)\{\sigma_1\varphi + \sigma_2\varphi^{1.5} + \sigma_3\varphi^3 + \sigma_4\varphi^{3.5}$$
$$+ \sigma_5\varphi^4 + \sigma_6\varphi^{7.5}\}, \tag{D3}$$

where T_c and P_c are critical values and $\varphi = 1 - T/T_c$, and

$$\rho_{ref}(T, m) - \rho_0(T) = \sum_{i=1}^{i=3}\alpha_{i0}m^{(i+1)/2} + \sum_{i=1}^{i=3}\sum_{j=1}^{j=3}\alpha_{ij}m^{(i+1)/2}$$
$$\times \left(\frac{T}{T_c}\right)^{(j+1)/2}, \tag{D4}$$

$$B(T, m) = \sum_{i=0}^{i=1}\sum_{j=0}^{j=3}\beta_{ij}m^i\left(\frac{T}{T_c}\right)^j, \tag{D5}$$

$$C(m) = \gamma_0 + \gamma_1 m + \gamma_2 m^{1.5}, \tag{D6}$$

$$\frac{\rho_0(T)}{\rho_c} = 1 + c_1\varphi^{1/3} + c_2\varphi^{2/3} + c_3\varphi^{5/3}$$
$$+ c_4\varphi^{16/3} + c_5\varphi^{43/3} + c_6\varphi^{110/3}, \tag{D7}$$

where $c_1 = 1.992741$, $c_2 = 1.099653$, $c_3 = -0.510839$, $c_4 = -1.754935$, $c_5 = -45.517035$, $c_6 = 674694.45$, $\beta_{00} = -1622.40$, $\beta_{01} = 9383.80$, $\beta_{02} = -14893.80$, $\beta_{03} = 7309.10$, $\gamma_0 = 0.11725$, $\sigma_1 = -7.859518$, $\sigma_2 = 1.844083$, $\sigma_3 = -11.786650$, $\sigma_4 = 22.680741$, $\sigma_5 = -15.961872$, and $\sigma_6 = 1.801225$. Required parameters for NaCl and CaCl$_2$ are presented in Table VI.

APPENDIX E: PARTIAL MOLAR VOLUME OF CO$_2$ IN WATER

Partial molar volume values can be obtained from Garcia [90]:

$$V_{CO_2} = 37.51 - 9.585 \times 10^{-2}T + 8.740 \times 10^{-4}T^2$$
$$- 5.044 \times 10^{-7}T^3, \tag{E1}$$

where T is in degrees Celsius and V_{CO_2} is in cm^3/mol.

TABLE VI.   Parameters for the calculation of NaCl + CaCl$_2$ brine density.

Salt	α_{10}	α_{11}	α_{12}	α_{13}	α_{14}	α_{20}	α_{21}
NaCl	2863.158	-46844.356	120760.118	-116867.722	40285.426	-2000.028	34013.518
CaCl$_2$	2546.760	-39884.946	102056.957	-98403.334	33976.048	-1362.157	22785.572
Salt	α_{22}	α_{23}	α_{24}	α_{30}	α_{31}	α_{32}	α_{33}
NaCl	-88557.123	86351.784	-29910.216	413.046	-7125.857	18640.780	-18244.074
CaCl$_2$	-59216.108	57894.824	-20222.898	217.778	-3770.645	9908.135	-9793.484
Salt	α_{34}	β_{10}	β_{11}	β_{12}	β_{13}	γ_1	γ_2
NaCl	6335.275	241.57	-980.97	1482.31	-750.98	-0.00134	0.00056
CaCl$_2$	3455.587	307.24	-1259.10	2034.03	-1084.94	-0.00493	0.00231

[1] Charles A. Doswell III, The distinction between large-scale and mesoscale contribution to severe convection: A case study example, Weather Forecast. **2**, 3 (1987).

[2] Kevin Ivan Hodges and C. D. Thorncroft, Distribution and statistics of african mesoscale convective weather systems based on the isccp meteosat imagery, Mon. Weather Rev. **125**, 2821 (1997).

[3] John W. Elder, Steady free convection in a porous medium heated from below, J. Fluid Mech. **27**, 29 (1967).

[4] Michael Gurnis, Large-scale mantle convection and the aggregation and dispersal of supercontinents, Nature **332**, 695 (1988).

[5] Jochen Kämpf and Jan O. Backhaus, Shallow, brine-driven free convection in polar oceans: Nonhydrostatic numerical process studies, J. Geophys. Res.: Oceans **103**, 5577 (1998).

[6] Remke L. Van Dam, Craig T. Simmons, David W. Hyndman, and Warren W. Wood, Natural free convection in porous media: First field documentation in groundwater, Geophys. Res. Lett. **36**, 111403 (2009).

[7] Andrei G. Fedorov, and Raymond Viskanta, Turbulent natural convection heat transfer in an asymmetrically heated, vertical parallel-plate channel, Int. J. Heat Mass Transfer **40**, 3849 (1997).

[8] Cedric Rolin, Byeongseop Song, and Stephen R. Forrest, Mass Transport Through the Carrier Gas Boundary Layer in Organic Vapor Phase Deposition, Phys. Rev. Appl. **1**, 034002 (2014).

[9] Run Hu, Shiyao Huang, Meng Wang, Liliang Zhou, Xiayao Peng, and Xiaobing Luo, Binary Thermal Encoding by Energy Shielding and Harvesting Units, Phys. Rev. Appl. **10**, 054032 (2018).

[10] Jose Ordonez-Miranda, Transistorlike Device for Heating and Cooling Based on the Thermal Hysteresis of VO_2, Phys. Rev. Appl. **6**, 054003 (2016).

[11] Francisco Suárez, Scott W. Tyler, and Amy E. Childress, A fully coupled, transient double-diffusive convective model for salt-gradient solar ponds, Int. J. Heat Mass Transfer **53**, 1718 (2010).

[12] Matan Zehavi, Alicia Boymelgreen, and Gilad Yossifon, Competition Between Induced-Charge Electro-Osmosis and Electrothermal Effects at Low Frequencies Around a Weakly Polarizable Microchannel Corner, Phys. Rev. Appl. **5**, 044013 (2016).

[13] Adrian Bejan, and Khairy R. Khair, Heat and mass transfer by natural convection in a porous medium, Int. J. Heat Mass Transfer **28**, 909 (1985).

[14] Ping Cheng and W. J. Minkowycz, Free convection about a vertical flat plate embedded in a porous medium with application to heat transfer from a dike, J. Geophys. Res. **82**, 2040 (1977).

[15] M. A. Mansour and Sameh E. Ahmed, A numerical study on natural convection in porous media-filled an inclined triangular enclosure with heat sources using nanofluid in the presence of heat generation effect, Eng. Sci. Technol. Int. J. **18**, 485 (2015).

[16] IPCC, *Special Report on Carbon Dioxide Capture and Storage* (Cambridge University Press, Cambridge, UK, 2005).

[17] David P. Keller, Ellias Y. Feng, and Andreas Oschlies, Potential climate engineering effectiveness and side effects during a high carbon dioxide-emission scenario, Nat. Commun. **5**, 3304 (2014).

[18] M. L. Szulczewski, M. A. Hesse, and R. Juanes, Carbon dioxide dissolution in structural and stratigraphic traps, J. Fluid Mech. **736**, 287 (2013).

[19] Mohamad R. Soltanian, Mohammad A. Amooie, David R. Cole, Thomas H. Darrah, David E. Graham, Susan M. Pfiffner, Tommy J. Phelps, and Joachim Moortgat, Impacts of methane on carbon dioxide storage in brine formations, Groundwater **56**, 176 (2018).

[20] Mohammad Javaheri, Jalal Abedi, and Hassan Hassanzadeh, Linear stability analysis of double-diffusive convection in porous media, with application to geological storage of CO_2, Transp. Porous Med. **84**, 441 (2010).

[21] Mario J. Martinez and Marc A. Hesse, Two-phase convective CO_2 dissolution in saline aquifers, Water Resour. Res. **52**, 585 (2016).

[22] Mohamad Reza Soltanian, Mohammad Amin Amooie, David R. Cole, David E. Graham, Seyyed Abolfazl Hosseini, Susan Hovorka, Susan M. Pfiffner, Tommy J. Phelps, and Joachim Moortgat, Simulating the cranfield geological carbon sequestration project with high-resolution static models and an accurate equation of state, Int. J. Greenh. Gas Con. **54**, 282 (2016).

[23] Dennis L. Newell, J. William Carey, Scott N. Backhaus, and Peter Lichtner, Experimental study of gravitational mixing of supercritical CO_2, Int. J. Greenh. Gas Con. **71**, 62 (2018).

[24] Z. Shi, B. Wen, M. A. Hesse, T. T. Tsotsis, and K. Jessen, Measurement and modeling of CO_2 mass transfer in brine at reservoir conditions, Adv. Water Resour. **113**, 100 (2018).

[25] Zhenxue Dai, Ye Zhang, Jeffrey Bielicki, Mohammad Amin Amooie, Mingkan Zhang, Changbing Yang, Youqin Zou, William Ampomah, Ting Xiao, Wei Jai *et al.*, Heterogeneity-assisted carbon dioxide storage in marine sediments, Appl. Energy **225**, 876 (2018).

[26] Mohamad Reza Soltanian, Mohammad Amin Amooie, Zhenxue Dai, David Cole, and Joachim Moortgat, Critical dynamics of gravito-convective mixing in geological carbon sequestration, Sci. Rep. **6**, 35921 (2016).

[27] Mohamad Reza Soltanian, Mohammad Amin Amooie, Naum Gershenzon, Zhenxue Dai, Robert Ritzi, Fengyang Xiong, David Cole, and Joachim Moortgat, Dissolution trapping of carbon dioxide in heterogeneous aquifers, Environ. Sci. Technol. **51**, 7732 (2017).

[28] H. Hassanzadeh, M. Pooladi-Darvish, D. W. Keith*et al.* , Modelling of convective mixing in CO storage, J. Can. Petrol. Technol. **44** (2005).

[29] Hassan Hassanzadeh, Mehran Pooladi-Darvish, and David W. Keith, Scaling behavior of convective mixing, with application to geological storage of CO_2, AIChE J. **53**, 1121 (2007).

[30] Rouhollah Farajzadeh, Hamidreza Salimi, Pacelli L. J. Zitha, and Hans Bruining, Numerical simulation of density-driven natural convection in porous media with application for CO_2 injection projects, Int. J. Heat Mass Transfer **50**, 5054 (2007).

[31] Hamid Emami-Meybodi, Hassan Hassanzadeh, Christopher P. Green, and Jonathan Ennis-King, Convective

dissolution of CO_2 in saline aquifers: Progress in modeling and experiments, Int. J. Greenh. Gas Con. **40**, 238 (2015).

[32] Mohammad Amin Amooie, Mohamad Reza Soltanian, and Joachim Moortgat, Hydrothermodynamic mixing of fluids across phases in porous media, Geophys. Res. Lett. **44**, 3624 (2017).

[33] Mohammad Amin Amooie, Mohamad Reza Soltanian, Fengyang Xiong, Zhenxue Dai, and Joachim Moortgat, Mixing and spreading of multiphase fluids in heterogeneous bimodal porous media, Geomech. Geophys. Geo-energ. Geo-resour. **3**, 225 (2017).

[34] Scott Backhaus, Konstantin Turitsyn, and R. E. Ecke, Convective Instability and Mass Transport of Diffusion Layers in a Hele-Shaw Geometry, Phys. Rev. Lett. **106**, 104501 (2011).

[35] Juan J. Hidalgo, Jaime Fe, Luis Cueto-Felgueroso, and Ruben Juanes, Scaling of Convective Mixing in Porous Media, Phys. Rev. Lett. **109**, 264503 (2012).

[36] Seyed Mostafa Jafari Raad and Hassan Hassanzadeh, Onset of dissolution-driven instabilities in fluids with nonmonotonic density profile, Phys. Rev. E **92**, 053023 (2015).

[37] A. Riaz, M. Hesse, H. A. Tchelepi, and F. M. Orr, Onset of convection in a gravitationally unstable diffusive boundary layer in porous media, J. Fluid Mech. **548**, 87 (2006).

[38] George S. H. Pau, John B. Bell, Karsten Pruess, Ann S. Almgren, Michael J. Lijewski, and Keni Zhang, High-resolution simulation and characterization of density-driven flow in CO_2 storage in saline aquifers, Adv. Water Resour. **33**, 443 (2010).

[39] Anja C. Slim, M. M. Bandi, Joel C. Miller, and L. Mahadevan, Dissolution-driven convection in a Hele–Shaw cell, Phys. Fluids **25**, 024101 (2013).

[40] Marco De Paoli, Francesco Zonta, and Alfredo Soldati, Dissolution in anisotropic porous media: Modeling convection regimes from onset to shutdown, Phys. Fluids **29**, 026601 (2017).

[41] Mohammad Amin Amooie, Mohamad Reza Soltanian, and Joachim Moortgat, Solutal convection in porous media: Comparison between boundary conditions of constant concentration and constant flux, Phys. Rev. E **98**, 033118 (2018).

[42] Anja C. Slim, Solutal-convection regimes in a two-dimensional porous medium, J. Fluid Mech. **741**, 461 (2014).

[43] Baole Wen, Daria Akhbari, Li Zhang, and Marc A. Hesse, Convective carbon dioxide dissolution in a closed porous medium at low pressure, J. Fluid Mech. **854**, 56 (2018).

[44] Amir Riaz and Yildiray Cinar, Carbon dioxide sequestration in saline formations: Part I–review of the modeling of solubility trapping, J. Pet. Sci. Eng. **124**, 367 (2014).

[45] Marc Andre Hesse, *Mathematical Modeling and Multiscale Simulation of Carbon Dioxide Storage in Saline Aquifers* (Stanford University, 2008).

[46] Jerome A. Neufeld, Marc A. Hesse, Amir Riaz, Mark A. Hallworth, Hamdi A. Tchelepi, and Herbert E. Huppert, Convective dissolution of carbon dioxide in saline aquifers, Geophys. Res. Lett. **37**, 22404 (2010).

[47] Maria Teres Elenius and Klaus Johannsen, On the time scales of nonlinear instability in miscible displacement porous media flow, Comput. Geosci. **16**, 901 (2012).

[48] R. Farajzadeh, B. Meulenbroek, D. Daniel, A. Riaz, and J. Bruining, An empirical theory for gravitationally unstable flow in porous media, Comput. Geosci. **17**, 515 (2013).

[49] Peichun A. Tsai, Kathleen Riesing, and Howard A. Stone, Density-driven convection enhanced by an inclined boundary: Implications for geological CO_2 storage, Phys. Rev. E **87**, 011003 (2013).

[50] Maria T. Elenius, Jan M. Nordbotten, and Henrik Kalisch, Convective mixing influenced by the capillary transition zone, Comput. Geosci. **18**, 417 (2014).

[51] Christopher P. Green and Jonathan Ennis-King, Steady dissolution rate due to convective mixing in anisotropic porous media, Adv. Water Resour. **73**, 65 (2014).

[52] Seyyedi Mojtaba, Rostami Behzad, Nazari Moghaddam Rasoul, and Rezai Mohammad, Experimental study of density-driven convection effects on CO_2 dissolution rate in formation water for geological storage, J. Nat. Gas Sci. Eng. **21**, 600 (2014).

[53] Lei Wang, Akimitsu Hyodo, Shigeki Sakai, and Tetsuya Suekane, Three-dimensional visualization of natural convection in porous media, Energy Proc. **86**, 460 (2016).

[54] Amir Taheri, Erik Lindeberg, Ole Torsæter, and Dag Wessel-Berg, Qualitative and quantitative experimental study of convective mixing process during storage of CO_2 in homogeneous saline aquifers, Int. J. Greenh. Gas Con. **66**, 159 (2017).

[55] Rasoul Nazari Moghaddam, Behzad Rostami, Peyman Pourafshary, and Yaser Fallahzadeh, Quantification of density-driven natural convection for dissolution mechanism in CO_2 sequestration, Transp. Porous Media **92**, 439 (2012).

[56] Timothy J. Kneafsey and Karsten Pruess, Laboratory flow experiments for visualizing carbon dioxide-induced, density-driven brine convection, Transp. Porous Media **82**, 123 (2010).

[57] Daria Akhbari, and Marc A. Hesse, Causes of under-pressure in natural CO_2 reservoirs and implications for geological storage, Geology **45**, 47 (2017).

[58] Duncan R. Hewitt, Jerome A. Neufeld, and John R. Lister, Convective shutdown in a porous medium at high rayleigh number, J. Fluid Mech. **719**, 551 (2013).

[59] C. A. Aggelopoulos, M. Robin, and O. Vizika, Interfacial tension between CO_2 and brine $(NaCl + CaCl_2)$ at elevated pressures and temperatures: The additive effect of different salts, Adv. Water Resour. **34**, 505 (2011).

[60] Tristan P. Wellman, Reid B. Grigg, Brian J. McPherson, Robert K. Svec, and Peter C. Lichtner *et al.*, in *SPE-International Symposium on Oilfield Chemistry* (Society of Petroleum Engineers, Houston, Texas, 2003).

[61] Irina Gaus, Mohamed Azaroual, and Isabelle Czernichowski-Lauriol, Reactive transport modelling of the impact of CO_2 injection on the clayey cap rock at sleipner (North Sea), Chem. Geol. **217**, 319 (2005).

[62] Tianfu Xu, Eric Sonnenthal, Nicolas Spycher, and Karsten Pruess, Toughreact–a simulation program for non-isothermal multiphase reactive geochemical transport in variably saturated geologic media: applications to geothermal injectivity and CO_2 geological sequestration, Comput. Geosci. **32**, 145 (2006).

[63] Diana H. Bacon, Bruce M. Sass, Mohit Bhargava, Joel Sminchak, and Neeraj Gupta, Reactive transport modeling of CO_2 and SO_2 injection into deep saline formations and their effect on the hydraulic properties of host rocks, Energy Proc. **1**, 3283 (2009).

[64] Reza Azin, Mohamad Mahmoudy, Seyed Mostafa Jafari Raad, and Shahriar Osfouri, Measurement and modeling of CO_2 diffusion coefficient in saline aquifer at reservoir conditions, Cent. Eur. J. Eng. **3**, 585 (2013).

[65] Ibrahim Mohamed, Jia He, and Hisham A. Nasr-El-Din, Effect of brine composition on CO_2/limestone rock interactions during CO_2 sequestration, J. Petrol. Sci. Res. **2**, 14 (2013).

[66] Hong Phuc Vu, Jay R. Black, and Ralf R. Haese, Changes in formation water composition during water storage at surface and post re-injection, Energy Proc. **114**, 5732 (2017).

[67] Barbara Cantucci, Giordano Montegrossi, Orlando Vaselli, Franco Tassi, Fedora Quattrocchi, and Ernie H. Perkins, Geochemical modeling of CO_2 storage in deep reservoirs: The weyburn project (Canada) case study, Chem. Geol. **265**, 181 (2009).

[68] Kevin G. Knauss, James W. Johnson, and Carl I. Steefel, Evaluation of the impact of CO_2, co-contaminant gas, aqueous fluid and reservoir rock interactions on the geologic sequestration of CO_2, Chem. Geol. **217**, 339 (2005).

[69] Rebecca Liyanage, Jiajun Cen, Samuel Krevor, John P. Crawshaw, and Ronny Pini, Multidimensional observations of dissolution-driven convection in simple porous media using x-ray ct scanning, Transp. Porous Media **126**, 355 (2019).

[70] Michael L. Szulczewski, Christopher W. MacMinn, Howard J. Herzog, and Ruben Juanes, Lifetime of carbon capture and storage as a climate-change mitigation technology, Proc. Natl. Acad. Sci. **109**, 5185 (2012).

[71] Saeed Mahmoodpour, Behzad Rostami, and Hamid Emami-Meybodi, Onset of convection controlled by N_2 impurity during CO_2 storage in saline aquifers, Int. J. Greenh. Gas Con. **79**, 234 (2018).

[72] Saeed Mahmoodpour and Behzad Rostami, Design-of-experiment-based proxy models for the estimation of the amount of dissolved CO_2 in brine: A tool for screening of candidate aquifers in geo-sequestration, Int. J. Greenh. Gas Con. **56**, 261 (2017).

[73] Duan Zhenhao and Rui Sun, An improved model calculating CO_2 solubility in pure water and aqueous nacl solutions from 273 to 533 K and from 0 to 2000 bar, Chem. Geol. **193**, 257 (2003).

[74] Ding-Yu Peng and Donald B. Robinson, A new two-constant equation of state, Ind. Eng. Chem. Fundam. **15**, 59 (1976).

[75] Zhenhao Duan, Rui Sun, Chen Zhu, and I-Ming Chou, An improved model for the calculation of CO_2 solubility in aqueous solutions containing Na^+, K^+, Ca^{2+}, Mg^{2+}, Cl^-, and SO_4^{2-}, Mar. Chem. **98**, 131 (2006).

[76] C. T. Tan and G. M. Homsy, Simulation of nonlinear viscous fingering in miscible displacement, Phys. Fluids **31**, 1330 (1988).

[77] W. B. Zimmerman and G. M. Homsy, Nonlinear viscous fingering in miscible displacement with anisotropic dispersion, Phys. Fluids **3**, 1859 (1991).

[78] W. B. Zimmerman and G. M. Homsy, Viscous fingering in miscible displacements: Unification of effects of viscosity contrast, anisotropic dispersion, and velocity dependence of dispersion on nonlinear finger propagation, Phys. Fluids **4**, 2348 (1992).

[79] Karim Ghesmat and Jalel Azaiez, Viscous fingering instability in porous media: Effect of anisotropic velocity-dependent dispersion tensor, Transp. Porous Med. **73**, 297 (2008).

[80] Panneerselvam Ranganathan, Rouhollah Farajzadeh, Hans Bruining, and Pacelli L. J. Zitha, Numerical simulation of natural convection in heterogeneous porous media for CO_2 geological storage, Transp. Porous Med. **95**, 25 (2012).

[81] Nasser Sabet, Seyed Mostafa Jafari Raad, Hassan Hassanzadeh, and Jalal Abedi, Dynamics of Miscible Nanocatalytic Reactive Flows in Porous Media, Phys. Rev. Appl. **10**, 054033 (2018).

[82] Tanguy Le Borgne, Timothy R. Ginn, and Marco Dentz, Impact of fluid deformation on mixing-induced chemical reactions in heterogeneous flows, Geophys. Res. Lett. **41**, 7898 (2014).

[83] Shahin Zarghami, Fathi Boukadi, and Yahya Al-Wahaibi, Diffusion of carbon dioxide in formation water as a result of CO_2 enhanced oil recovery and CO_2 sequestration, J. Petrol. Explor. Prod. Technol. **7**, 161 (2017).

[84] C. R. Wilke and Pin Chang, Correlation of diffusion coefficients in dilute solutions, AIChE J. **1**, 264 (1955).

[85] Saeed Mahmoodpour, Behzad Rostami, Mohamad Reza Soltanian, and Mohammad Amin Amooie, Effect of brine composition on the onset of convection during CO_2 dissolution in brine, Comput. Geosci. **124**, 1 (2019).

[86] Shide Mao and Zhenhao Duan, The viscosity of aqueous alkali-chloride solutions up to 623 K, 1,000 bar, and high ionic strength, Int. J. Thermophys. **30**, 1510 (2009).

[87] Hai-Lang Zhang, Geng-Hua Chen, and Shi-Jun Han, Viscosity and density of $H_2O + NaCl + CaCl_2$ and $H_2O + KCl + CaCl_2$ at 298.15 K, J. Chem. Eng. Data **42**, 526 (1997).

[88] Robert W. Potter and David L. Brown, *The Volumetric Properties of Aqueous Sodium Chloride Solutions from 0 to 500 °C at Pressures up to 2000 bars Based on a Regression of Available Data in the Literature* (US Government Printing Office, 1977).

[89] Saif Al Ghafri, Geoffrey C. Maitland, and J. P. Martin Trusler, Densities of aqueous $MgCl_2(aq)$, $CaCl_2(aq)$, $KI(aq)$, $NaCl(aq)$, $KCl(aq)$, $AlCl_3(aq)$, and $(0.964 NaCl + 0.136 KCl)(aq)$ at temperatures between (283 and 472) K, pressures up to 68.5 MPa, and molalities up to $6 mol \cdot kg^{-1}$, J. Chem. Eng. Data **57**, 1288 (2012).

[90] Julio E. Garcia, Lawrence Berkeley National Laboratory Report LBNL49023, Berkeley, CA (2001).